Boundary layer flow interaction with a permeable wall

Cite as: Phys. Fluids **30**, 085111 (2018); https://doi.org/10.1063/1.5043276
Submitted: 07 June 2018 . Accepted: 13 August 2018 . Published Online: 30 August 2018

Syamir Alihan Showkat Ali, Mahdi Azarpeyvand, Máté Szőke, and Carlos Roberto Ilário da Silva

Boundary layer flow interaction with a permeable wall

Syamir Alihan Showkat Ali,[1,2,a)] Mahdi Azarpeyvand,[1,b)] Máté Szőke,[1] and Carlos Roberto Ilário da Silva[3]
[1]*Faculty of Mechanical Engineering, University of Bristol, BS8 1TR Bristol, United Kingdom*
[2]*School of Manufacturing Engineering, University Malaysia Perlis, 02600 Perlis, Malaysia*
[3]*Embraer, São José dos Campos 12227-901, Brazil*

(Received 7 June 2018; accepted 13 August 2018; published online 30 August 2018)

The interaction of a zero pressure gradient turbulent boundary layer flow with a rough permeable surface has been investigated experimentally. The flow interaction characteristics have been examined using a long flat plate equipped with several surface pressure transducers and pressure taps. Three types of porous materials with different porosities and permeability constants were used in these investigations. To reveal the behavior of turbulent flows over porous surfaces, measurements were performed for the boundary layer growth, energy content of the turbulent structure within the boundary layer, and surface pressure fluctuations, before, over, and after the porous test-section. The interaction of the flow with the porous substrate was found to significantly alter the energy cascade within the boundary layer. Results have also shown that the boundary layer interaction with the rough porous surfaces leads to an increase in the pressure fluctuations exerted on the wall, particularly at low frequencies. The near-field investigations have shown that the penetration of the boundary layer flow into the porous medium can generate an internal hydrodynamic field within the porous medium. This, in turn, reduces the frequency-energy content of the large boundary layer coherent structures and their spanwise correlation length. This study paves the way for further investigation into the interaction of the porous media with different flow fields and development of tailored porous treatments for improving the aerodynamic and aeroacoustic performance of different aero- and hydro-components. *Published by AIP Publishing.* https://doi.org/10.1063/1.5043276

NOMENCLATURE

C_p	Pressure coefficient [$C_p = (p_i - p_\infty)/(0.5\rho U_\infty^2)$]
C_f	Skin friction coefficient
f	Frequency (Hz)
h_s	Sand height in the porous medium (mm)
L, W	Plate streamwise and spanwise lengths (mm)
l	Wire length (mm)
L_p, W_p	Porous section streamwise and spanwise lengths (mm)
p'	Fluctuating surface pressure (Pa)
p_i	Static pressure at the ith location (Pa)
p_∞	Free-stream static pressure at the ith location (Pa)
Ra	Average roughness (μm)
Re	Reynolds number
$R_{p'_i p'_j}$	Wall pressure cross-correlation coefficient between two pressure transducers
$R_{p'_i p'_i}$	Wall pressure autocorrelation
U_∞	Free stream velocity (m/s)
U	Mean velocity (m/s)
U_{rms}	Root mean square velocity (m/s)
U_c	Convection velocity (m/s)
u'	Streamwise fluctuating velocity (m/s)
u_τ	Wall friction velocity (m/s)
x, y, z	Cartesian coordinates (mm)
ρ	Fluid density (kg/m^3)
φ	Porosity (%)
κ	Permeability (m^2)
$\triangle p$	Pressure drop across the porous sample (Pa)
ν	Kinematic viscosity of air (m^2/s)
ν_D	Darcian velocity (m/s)
τ	Time delay (s)
δ	Boundary layer thickness (mm)
δ^*	Boundary layer displacement thickness (mm)
θ	Boundary layer momentum thickness (mm)
ϕ_{uu}	Power spectral density of velocity fluctuations (dB/Hz)
ϕ_{pp}	Power spectral density of pressure fluctuations (dB/Hz)
$\gamma^2_{p'_i p'_j}$	Wall pressure coherence between two pressure transducers
Λ_p	Spanwise coherence length (mm)
Φ	Cross-power spectral density function
ξ_x, ξ_y, ξ_z	Streamwise, vertical, and spanwise separation distance (mm)
PPI	Pores per inch
PSD	Power spectral density

I. INTRODUCTION

The possibility of controlling turbulent flows, reducing the energy content of flow structures, and suppressing aerodynamically generated noise at the source is of great academic and

a)Electronic mail: ss14494@bristol.ac.uk
b)Electronic mail: m.azarpeyvand@bristol.ac.uk

industrial interest. There are numerous studies on the development of bespoke passive and active techniques for the control of unsteady flows and their associated noise generation, such as serrations,[1–3] surface treatments,[4] porous treatments,[5–7] flow suction and blowing,[8] etc. The use of porous media, in particular, for the passive or semi-active control of flow-induced noise and vibrations and thermal purposes has received considerable academic and industrial attention over the past five decades. Examples include flow over heat and mass exchangers,[9] river beds,[10] bluff bodies,[6] airfoils,[11] forest canopies[12] or the network of urban canyons, transpiration cooling, convection and heat transfer in composite fluid and porous layers,[13] etc. Recent preliminary experimental and computational research on the application of porous treatments for different aero-structures, such as bluff bodies and airfoil trailing-edges, has shown that the use of porous treatments can suppress the aerodynamic noise by manipulating the flow through various mechanisms, such as preventing flow separation, changing the boundary layer shape, adjusting the pressure field beneath the boundary layer, and decreasing the wake and vortex shedding effects. To date, prior research in this area has shown that the careful implementation of porous treatments can lead to flow stabilization and reduction of the aerodynamically induced noise.

While much of the literature on this topic focuses on the universal aspects of the mean flow field and turbulent statistics over the porous wall, several studies have also been directed toward understanding the influence of permeability on fluid flows. Suga[14] carried out several experiments on the effects of a flow-permeable wall with a varying permeability value, but with similar porosity ($\varphi \approx 0.8$) using the Particle Image Velocimetry (PIV). The experiments were conducted at low Reynolds numbers ($Re \leqslant 10\,200$), and it was shown that the transition to turbulence occurs at a lower Reynolds number over the porous surface, with the increase in the permeability. The near-field wall velocity fluctuations were found to be higher with increasing permeability in the flow-vertical direction, which leads to higher shear stress at the porous surface. Recently, Manes *et al.*[15] showed that the flow resistance and the shear penetration on permeable walls increase with increasing the permeability (κ)-based Reynold's number Re_κ, where the penetration depth is defined as the inner length scales of the turbulent flows. It was observed that the rms of the streamwise velocity decreases at the near-wall region with increasing permeability and increases the energy content of the vertical velocity fluctuations and, correspondingly, the Reynolds shear stress. The results also showed that the boundary layer flow structures on the surfaces with higher permeability are influenced by an unstable mode of turbulent mixing layers which allows the production of the Kelvin-Helmholtz shear instabilities, while such instability eddies were not seen for the surfaces with low permeability. The shear instability was observed to dominate the near-wall flow structures, in the cases where the shear penetration depth is relatively larger than the boundary layer thickness. Breugem *et al.*[16] have studied the effect of the flow inside a permeable wall with different porosities (φ = 0.6, 0.8, and 0.95). It was shown that the mean velocity profile decreases significantly for the porous surface with higher porosity, and this was accompanied by a strong increase in the Reynolds shear stress near the porous wall. This results in an increase in the skin friction coefficient of about 30%, which is also evident in the experimental study by Kong and Schetz.[17] It was also found that the quasi-streamwise vortices and high-speed streaks observed near a solid wall have significantly weakened over the porous surface due to the reduction in the mean shear and in the wall-blocking effect while enhancing the turbulent transport across the porous medium. Breugem *et al.* also showed that the weakening of the vortices over the porous surface leads to a reduction in the streamwise rms velocity peak and an increase in the spanwise and vertical rms velocity peak, caused by the flow penetration in the porous medium. It has also been shown that the rms velocity profile inside the porous medium exhibits an exponential-like tail and that the turbulence motions established inside the porous are not responsible for the increase in the Reynolds shear stress near the porous wall.

In addition to the effects of permeability, the roughness of the porous surfaces has also been found to be a determining factor in the behavior of the flow over and past such surfaces. The mechanisms involved in the interaction of flows with rough and permeable surfaces, i.e., foams, perforated sheets, beds of packed spheres, etc., have been experimentally and numerically investigated in numerous studies.[12,14–22] Kong and Schetz[17] studied the effect of small-scale roughness and porosity through the development of the turbulent boundary layers over smooth, rough, and porous surfaces. They found that the porosity of the porous surface can generally shift the wall logarithmic region downward by $\Delta U^+ \approx 3$–4 compared to the smooth wall, leading to an increase of the skin friction values by about 30%–40%. It was also shown that the streamwise and vertical flow turbulence intensities and the Reynolds stress are increased in the boundary layer region, with a significant increase closer to the wall region. Jimenez *et al.*[19] studied the effect of porosity on a passive porous wall and its contribution in delaying the boundary layer separation. Results have shown a significant increase in the skin friction of about 40% at the porous walls, along with the presence of the local flow separation. This is due to the emergence of the large spanwise rollers, originating from the Kelvin-Helmholtz instability and the neutral inviscid shear waves of the mean velocity profile. Finnigan[12] studied the turbulent shear flows generated by a plant canopy, which resembles, to some extent, the flow over porous media and a rough-wall boundary layer. The results showed that the inflected velocity profile at the canopy top, unlike in a standard boundary layer profile, is exhibited by an inviscid instability mechanism and consequently generates more energetic coherent structures than that in the inertial sublayer or log-layer at transporting momentum. The influence of the vegetation density on the canopy sub-layer is later investigated by Poggi *et al.*,[18] and the results demonstrated that (a) the flow in the lowest layer within the canopy is dominated by small-scale von Karman vortices, (b) the flow is superimposed of a mixing layer and the wall roughness effect in the boundary layer in the middle layer of the canopy region, and (c) the upper layer of the canopy region can be expressed using the surface layer similarity theory. The use of micro-cavity array, as a passive flow control method, has also received much attention in recent years. The submilimeter micro-perforated panel

(MPP) has been used widely as the robust sound absorber in many applications. It was shown that this device can provide sufficient acoustic resistance and low acoustic mass reactance, which is fundamental for a wide-band sound absorber. Maa[23] has demonstrated the utilization of the submilimeter MPP to absorb sound by investigating the relationship between the perforation radius and the viscous boundary layer thickness. He found that the perforate constant is proportional to the ratio of the perforation radius to the viscous boundary layer thickness inside the holes, which can determine the characteristic of acoustic impedance and the frequency of the structure absorbed by the MPP. Silvestri *et al.*[24,25] have showed that the use of micro-cavity array on a flat-plate, which is an extension of the work conducted by Maa,[23] leads to significant reduction of the turbulence energy and the sweep intensity in the turbulent boundary layer. It was also shown that the use of the micro-cavities surface can dampen the coherent structures and disrupt the bursting cycle, responsible for the shear stress and the viscous drag in the inner region of the boundary layer. Results have also shown that the reduction in the turbulence intensity is significantly dependent on the volume of the cavity, where non-linear reduction in the turbulence intensity can be found with increasing cavity volume. The cavity array orifice length, on the other hand, was found to have negligible effects in the sweep intensity attenuation.

As reviewed above, despite a large body of the literature on the interaction of flow on rough permeable surfaces, there are only a few studies on the pressure fluctuations for boundary layers over rough[26–29] and porous[5] surfaces, which are of great importance for understanding the noise and vibration generation from such structures. Blake[26] studied the pressure fluctuations for turbulent boundary layers over smooth and different rough walls. It is claimed that the different roughness parameters, such as the roughness separation and height, affect the very large-scale structure and small-scale turbulence structure, respectively. It was also found that the coherence loss in the pressure eddies for rough walls is higher than that the smooth walls due to the high turbulence production rate near the surface. Varano,[27] on the other hand, investigated the rough surface with fetches of hemispherical roughness and found that the turbulent kinetic energy and shear stress production increase downstream of the element due to the delay in the flow separation over the top of the element. Bai *et al.*[30] studied the application of spanwise altering a roughness strip with two different roughness heights and showed that the large-scale counter-rotating roll-modes are observed over the rough wall, with reduced and increased streamwise velocities occurring over the low- and high-roughness strips, respectively. The results also indicated that pronounced modifications in the mean vorticities, swirling strength, and Reynolds stresses can be observed over the roughness strip. It was also found that a strong instantaneous turbulence event occurs over the rough wall, whose underlying mechanisms are still unclear. A recent effort by Meyers *et al.*[28] presented a comprehensive study on the wall pressure spectrum of a flat plate with smooth and rough walls with sparse arrays of different size and distribution of hemispherical bumps at high Reynolds numbers. The results showed that the boundary layers of both the rough and smooth surfaces have similar outer boundary layer scales at the low frequencies of the wall-pressure spectrum and have a universal viscous form at the higher frequency range. It was also confirmed that the friction velocity obtained in the case of rough-wall boundary layers is always less than the conventional friction velocity found for a smooth-wall boundary layer and confirmed that the boundary layer parameters and the wall pressure spectrum are nearly independent of the surface roughness for the conditions considered in the study. Building on the work of Meyers, Joseph *et al.*[29] have investigated rough walls with two fetches of hemispherical roughness elements with two different spacing ratios. It has been demonstrated that the pressure spectral shape changes at mid frequencies with the roughness density, and it was speculated that the spectral changes are not due to the changes in the turbulence structure but rather due to the displacement of the pressure fluctuations over the roughness elements. In a more recent study, Showkat Ali *et al.*[31] have shown that the use of porous treatments can lead to a significant reduction in the energy content of the large low-frequency boundary layer structures. It was also found that surfaces with high permeability are able to greatly alter the boundary layer and attenuate vortex shedding frequency. Moreover, results also showed that the spanwise coherence of the large coherent structures can be significantly reduced using high permeable materials.

Despite the promising success of porous materials and its relevance to the aforementioned applications, the boundary layer flow-porous interaction effects have rather received little attention. For instance, the majority of the existing experimental studies and numerical methods do not take all the flow-porous interaction aspects into accounts, such as the porous-flow viscous interaction, flow-porous roughness effect, flow penetration, and hydrodynamic absorption in the porous media, which have, to some extent, remained unclear. To address some of the limitations described above, detailed understanding of the underlying mechanisms of flow-porous control is imperative. To gain a proper understanding of such mechanisms, it is important to characterize the effects of porosity and permeability, as well as its morphological characteristics of the surface roughness simultaneously. Our main goal in this paper is to better understand the flow-porous boundary layer interaction. The interaction of the boundary layer with a porous surface can bring about changes to the boundary layer structure and the energy cascade within the boundary layer and the frequency-energy content of the large coherent structures within the boundary layer, mainly responsible for the generation of aerodynamic noise. A flat plate with smooth and varying porosities and permeabilities porous walls, equipped with several wall pressure transducers was designed and manufactured to investigate the interaction of fully turbulent flows with porous surfaces and its effects on the boundary layer development, surface pressure fluctuations, and, correspondingly, the noise generation. The paper is organized as follows. The experimental setup and wind-tunnel tests are described in Sec. II. The effect of the porous surface on the boundary layer and their energy content will be discussed in Sec. III. Section IV further discusses the dynamic pressure exerted on the surface with and without the porous substrates. A detailed analysis of the flow velocity and pressure correlation and coherence studies are presented in Sec. V. Section VI

further elaborates the formation of the internal hydrodynamic field and its dependency on the flow penetration length. Finally, Sec. VII concludes and summarizes our finding on the turbulent boundary layer flow-porous interaction.

II. MEASUREMENT SETUP

The flow experiments have been performed using a flat plate in the open jet wind tunnel facility of the University of Bristol; see Fig. 1. The wind tunnel has a test-section diameter of 1 m and working section length of 2 m. The results were obtained for the flow velocity of 20 m/s with a maximum incoming flow turbulence intensity of 0.5%. In order to properly understand the boundary layer interaction with porous surfaces, numerous measurements have been conducted, such as the boundary layer growth, surface pressure fluctuations, velocity-pressure coherence and correlations, and spanwise length scales. The experimental setup and the measurement techniques used in this study are explained in Subsections II A–II D.

A. Flat plate configuration

The flow measurements have been performed using a flat plate with a streamwise length of L = 1500 mm, spanwise length of W = 715 mm, and thickness of h = 20 mm. The general layout of the flat plate test-rig is shown in Fig. 1(a). In order to prevent flow separation and the strong adverse pressure gradient, the flat plate was designed with an elliptical leading-edge with a semi-minor and semi-major axis of 10 mm and 27 mm, respectively. The coordinate system (x, y, z) is placed at the beginning of the porous section, as illustrated in Fig. 1(a). To realize a zero-pressure gradient turbulent boundary layer on the top side of the plate, particularly near to the trailing-edge, a 12° beveled trailing-edge was employed.[32] In addition, to ensure the zero-pressure gradient condition on the plate, static pressure measurements along the flat plate, after the test section region, were conducted using 12 static pressure ports within x = 160 mm–240 mm at the free-stream velocity of 20 m/s. The static pressure measurements were performed using a 32 channel Chell MicroDaq Smart Pressure Scanner. The scanner is able to measure the pressure difference of up to 1 psi, with the system accuracy of ±0.05% full-scale. The static pressure data for the flat plate test rig were acquired for 60 s at the maximum sampling frequency of 500 Hz. The accuracy of the pressure measurements carried out for the flat plate was below 5 Pa. Figure 2 shows that the pressure coefficient C_p distributions along the flat plate are constant within the uncertainty levels of 2σ = ±0.97% at 95% confidence level, indicating the absence of the pressure gradient along the plate. A 100 mm wide section of 80 grit sand trip, equivalent to the average roughness of R_a = 1.8 μm, was applied at 120 mm after the leading-edge, on the top side of the plate, to ensure a well-developed turbulent flow transition before the porous section (x = 0). The porous section is placed in a cavity space, 840 mm downstream of the plate leading-edge with a streamwise length L_p of 120 mm, width W_p of 560 mm, and depth h of 20 mm. Great care was taken to ensure that the porous insert does not cause any geometrical step. Figure 1(b) provides a schematic of the porous insert installation. An 18 mm wide solid wedge is placed on either sides of the porous insert to avoid any possible flow separation at the porous-solid interface (x = 0 and x = 120 mm). In order to avoid air bleeding through the porous inserts, the bottom part of the porous samples was covered and sealed using a solid medium density fibre (MDF) sheet. Four metal foams with the PPI (pores per inch) of 25, 35, 45, and 80 were used for this study.

B. Porous material characterization

Four uncompressed metal foams with PPI (pores per inch) values of 25, 35, 45, and 80 have been chosen for this study.

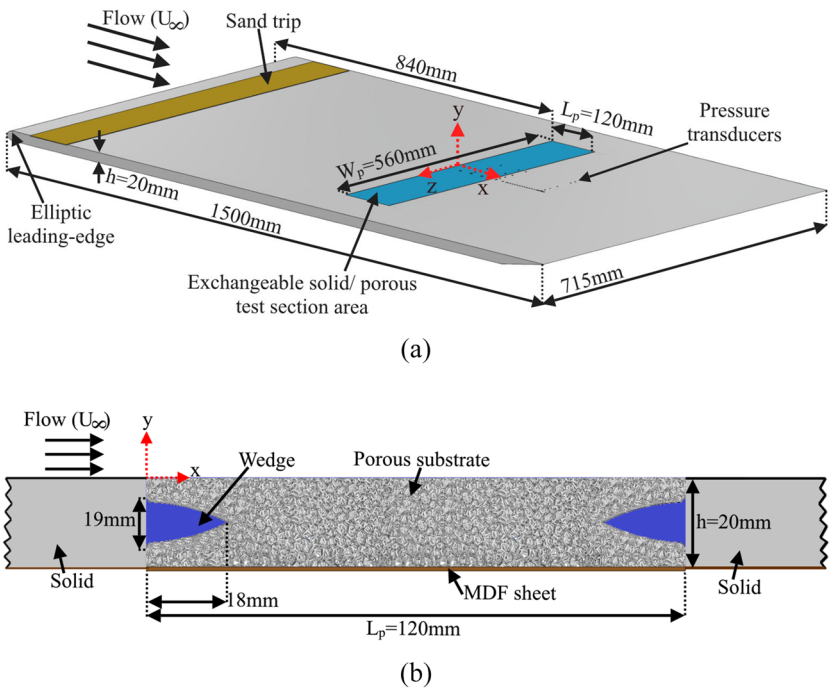

FIG. 1. (a) Flat plate experimental setup and (b) illustration of the porous substrate installation.

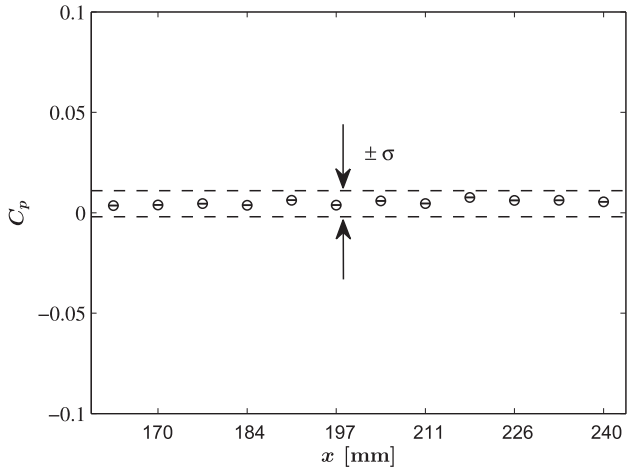

FIG. 2. Pressure distribution (C_p) in the streamwise direction within x = 160 mm–240 mm for the flat plate with a fully solid surface at the free-stream velocity of 20 m/s.

The 3*D* images of the porous materials used are shown in Fig. 3(a). The effectiveness of porous treatments as a flow and noise control technique relies greatly on the porosity (φ) and permeability (κ) of the material.[33–36] Given the importance of these two quantities, especially in the context of flow and noise control, both parameters have been measured for the porous samples studied here. The porosity of a porous medium is a measure of the proportion of the total volume of the material occupied by pores. The inner structure of the porous samples was captured using a Nikon XT H 320 LC computed tomography scanner non-intrusively with great precision, and the data obtained were then analyzed using the VGStudio MAX 2.2 software. The porosity, φ, can then be calculated from $\varphi = V_V/V_T$, where V_V and V_T correspond to the volume of void space and the total volume of the sample, respectively. The porosity values for porous 25 PPI, 35 PPI, 45 PPI, and 80 PPI are 90.92%, 88.39%, 85.37%, and 74.76%, respectively.

The permeability (κ) is the property of a porous material that enables fluids to penetrate through it. The permeability measurement of each porous material was carried out using a permeability test rig made of a 2.5 m long square cross section tube, equipped with several static and total pressure measurement points. The permeability tests were conducted on samples of the porous materials with a cross section of 80 × 80 mm and thickness of 10 mm, placed 1.2 m from the inlet of the long permeability test-rig. The pressure drop across the sample obtained from the static pressure taps, flush mounted on either side of the porous sample, were measured using the MicroDaq Smart Pressure Scanner 32C. The static pressure data for the permeability measurements were acquired for 60 s, with a sampling frequency of 500 Hz. The permeability coefficient κ is calculated using the Dupuit-Forchheimer equation[37] $\triangle p/t = \mu/\kappa v_D + \rho C v_D^2$, where $\triangle p$ is the pressure drop across the sample, t is the sample thickness, ρ is the fluid density, C is the inertial loss term, v_D is the Darcian velocity, which represents as the volume flow rate divided by cross sectional area of the sample. The permeability values for porous 25 PPI, 35 PPI, 45 PPI, and 80 PPI are found to be 8.2×10^{-8} m^2, 4.4×10^{-8} m^2, 2.1×10^{-8} m^2, and 7.7×10^{-9} m^2, respectively.

The morphology of the porous surface, particularly the surface roughness, is also found to be a crucial factor in characterizing the porous materials. The roughness of the porous surfaces was measured using a high-resolution non-contact profilometer Scantron Proscan 2100 analysis tool. All the data obtained were then visualized and analyzed using the Proform software module, and the data collected are then reproduced using the Matlab software. The average roughness parameter, R_a, can be calculated as the arithmetic mean of the absolute values of the profile deviations (y_i) from the mean line of the roughness profile as $R_a = 1/L_s \sum_{i=1}^{L_s} |y_i|$, where L_s is the number of data points within the profile evaluation length or the sampling length and y_i is the profile height function or the variation of the vertical distance from the mean surface line to the ith data point. The average roughness values for porous 25 PPI, 35 PPI, 45 PPI, and 80 PPI are found to be 1922 μm, 1791 μm, 1761 μm, and 212 μm, respectively. The permeability and the roughness of the four porous materials used in this study based on the measured porosity of the uncompressed metal samples are shown in Fig. 3(b). Results have shown that the porous samples with larger permeability and porosity

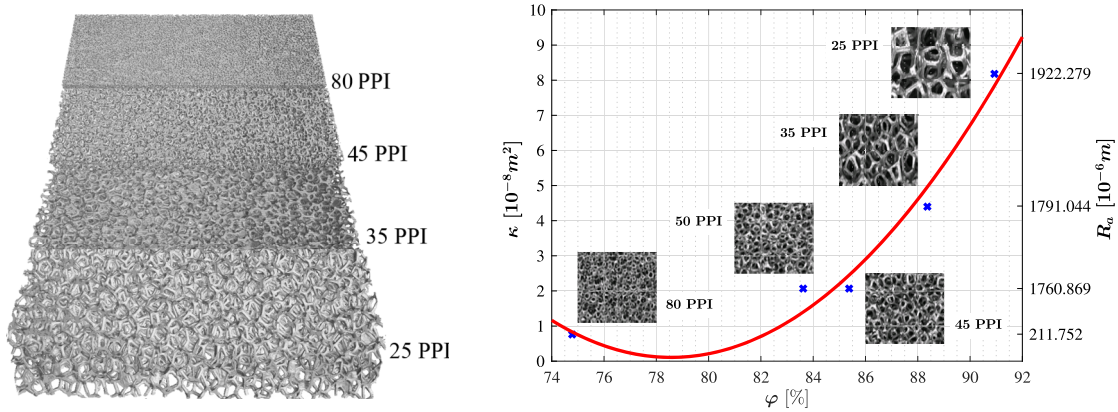

FIG. 3. (a) Uncompressed metal foams used in this study and (b) permeability and surface roughness as a function of porosity.

TABLE I. Positions of the pinhole transducers in the streamwise direction over and after the porous test-section.

Section	Transducer number, p	Axial locations, x (mm)
Porous/solid (x = 0 mm–120 mm)	1, 2, 3, 8, 9, 10, 11	30, 33, 60, 63, 90, 93, 110
Solid (x > 120 mm)	16, 21, 22, 23, 24, 25, 26, 27, 28, 29, 30, 31, 32, 33, 34, 35, 40, 41	130, 150, 165, 171, 178, 185, 191, 198, 205, 212, 217, 225, 232, 234, 249, 255, 262, 266

are associated with a higher surface roughness. In this paper, the flow measurement results will only be presented for the porous materials with 25, 45, and 80 PPI, as the 35 PPI material was found to give very similar results to that of the 25 PPI material.

C. Hot-wire anemometry setup

In order to measure the turbulent properties of the flow, the boundary layer measurements were carried out using a single hot-wire Dantec 55P16 probe, with a platinum-plated tungsten wire of 5 μm diameter and 1.25 mm length, giving a length-to-diameter (l/d) ratio of 250 with good spatial resolution and high-frequency response. These correspond to the viscous length scale (ν/u_τ) of 16.25 μm, viscous-scaled wire length l^+ of 64.1, and viscous-scaled wire diameter d^+ of 0.25. Ligrani and Bradshaw's[38] criterion for $l/d > 200$ has therefore been complied to in the present study, which provides sufficient sensitivity in measuring the velocity (mean and fluctuations) with minimal thermal effects. The probe was operated by a Dantec StreamlinePro frame, and the signals collected were low-pass filtered with a corner frequency of 30 kHz and an overheat ratio of 0.8.[39] The data have been acquired using a National Instrument PXIe-4499, with a sampling frequency f_s of 2^{16} Hz, and the signals were recorded for 16 s at each location, which equates to a viscous-scale sample interval of $\Delta t^+ = 0.62$ ($\Delta t^+ = \Delta t u_\tau^2/\nu$, where $\Delta t = 1/f_s$). This sample interval exceeds the minimum time scale ($t^+ \gtrsim 3$) for energetic turbulent fluctuations.[40] The boundary layer measurement was repeated three times at a sampling frequency of 2^{16} for 16 s at each location to ensure repeatability. The sampling parameters chosen were sufficient for the convergence of the velocity statistics, power spectral density, coherence, and correlation measurements. The probe was calibrated using the Dantec 54H10 type calibrator, before and after each measurement. The uncertainty of the velocity signals was calculated using the manufacturer's method[39] and was found to be within 1%. A two-axis (x-y) The ThorLabs LTS300M traverse system was used to move the probe in the flow, covering a 300 mm × 300 mm domain with a typical minimum positioning accuracy of ±5 μm.

D. Surface pressure measurement setup

The plate was instrumented with 41 miniature pressure transducers (Knowles FG-23329-P07) for the measurement of the unsteady boundary layer surface pressure fluctuations. The transducers are 2.5 mm in diameter, have a circular sensing area of 0.8 mm, and were positioned under a pinhole mask of 0.4 mm diameter to avoid pressure attenuation at high frequencies.[41] In order to avoid attenuation of the pressure at high frequencies due to sensing area pressure averaging, the pinhole non-dimensional diameter ($d^+ = du_\tau/\nu$)[42] should be in the range of $12 < d^+ < 18$ for frequencies up to $f^+ = f\nu/u_\tau^2 = 1$. The pinhole mask used for this study gives a non-dimensionalized diameter of $d^+ \approx 18.67$, which is close to the pinhole diameter range suggested by Gravante.[42] The surface pressure measurement data obtained give an absolute uncertainty of ±0.5 dB with 99% of confidence level. The transducers were installed inside the plate parallel to the surface and were distributed over and downstream of the porous section. The transducers are arranged in the form of L-shaped arrays in the streamwise and spanwise directions. A total number of four spanwise locations, each with five transducers, are used to calculate the spanwise coherence and coherence length of the boundary layer coherent structures over and at the downstream locations of the porous surfaces, while the transducers located in the streamwise direction will be used to study the changes of the boundary layer structures as they travel downstream over the porous section and their associated convection velocity. The surface pressure fluctuation data have been acquired using a National Instrument PXIe-4499, with a sampling frequency of 2^{16} Hz and measurement time of 60 s. The pressure transducer locations in the streamwise and spanwise directions on the flat plate over and after the porous test section are detailed in Tables I and II, respectively.

III. BOUNDARY LAYER FLOW STRUCTURES

While in many applications, such as low drag surfaces, flow laminarization, etc., it is common to present the boundary layer results in wall units format, i.e., normalized by quantities such as y^+, u^+, u_τ, etc., in applications relevant to aerodynamic noise generation, and we are often interested in the overall size of the boundary layer. The boundary layer and hydrodynamic results in most studies in the areas of aerodynamic

TABLE II. Positions of the pinhole transducers in the spanwise direction over and after the porous test-section.

Section	Transducer number, p	Axial locations, x (mm)	Transverse locations, z (mm)
Porous/solid (x = 0 mm–120 mm)	3, 4, 5, 6, 7	60	0, 3.2, 11.4, 24.2, 42.6
	11, 12, 13, 14, 15	110	
Solid (x > 120 mm)	16, 17, 18, 19, 20	130	
	35, 36, 37, 38, 39	255	

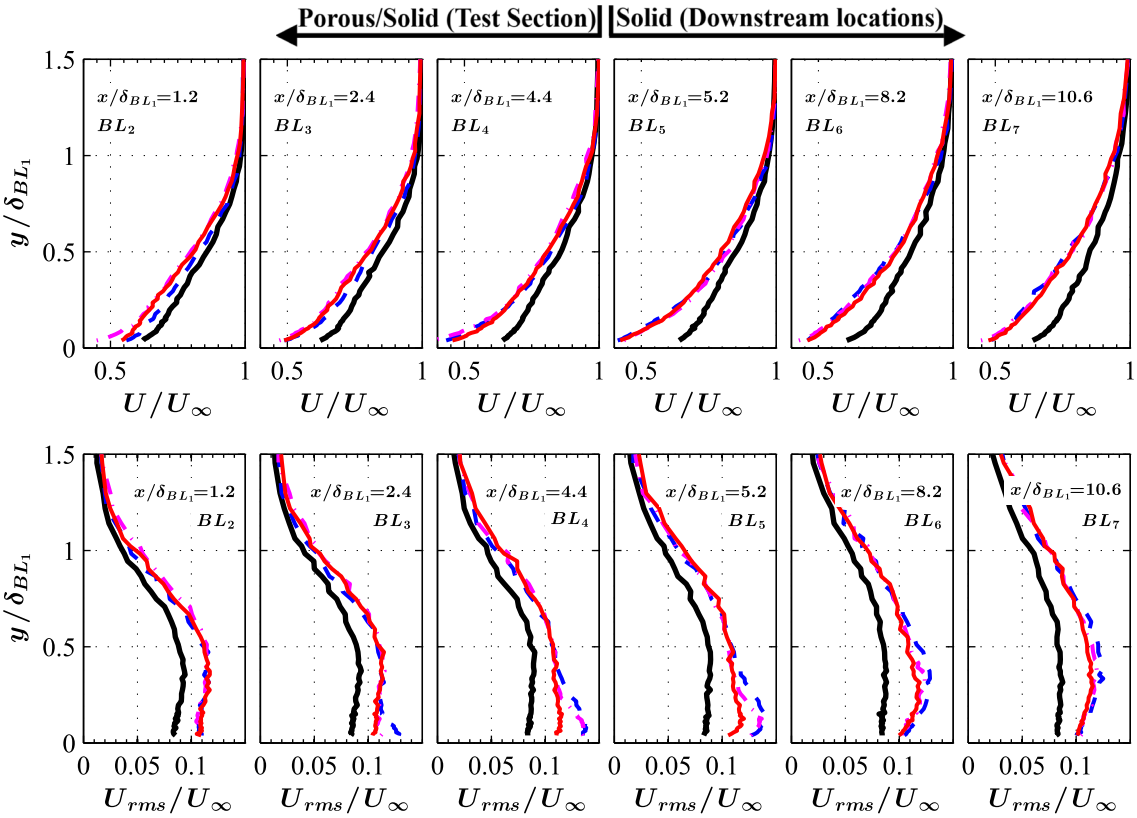

FIG. 4. Boundary layer mean and RMS velocity profiles at different streamwise locations over the flat plate. *Solid* (black solid curve), *porous* 80 *PPI* (red solid curve), *porous* 45 *PPI* (pink dotted-dashed curve), and *porous* 25 *PPI* (blue short-dashed curve).

noise generation and control are, therefore, presented in terms of the overall boundary layer thickness quantities, such as the boundary layer, displacement, or momentum thickness, particularly when the low frequency aspect of the noise generation is of concern. However, in order to ensure that the flat plate test rig developed as part of this study provides a standard zero pressure gradient boundary layer, the series of thorough measurements had been carried out prior to the actual tests using only the solid surfaces. The validation test matrix included $y^+ - u^+$ and the surface pressure fluctuation ϕ_{pp}. The $y^+ - u^+$ results had been compared and validated against the prior experimental[24,43] and DNS[44] data and good agreement was found. The surface pressure fluctuation results were also checked against the Goody model for a zero pressure gradient flat plate case[45] and good agreement was obtained. The validation results are not presented for the sake of brevity.

To better understand the boundary layer flow structures and the effect of the porous surfaces, the boundary layer velocity and the energy content of the boundary layer flow structures are studied in this section. Figure 4 presents the normalized time-averaged mean and root-mean-square (rms) boundary layer velocity profiles at various streamwise locations (BL_2–BL_7), as shown in Fig. 5.

The boundary layer integral parameters including the boundary layer thickness (δ), displacement thickness (δ^*), momentum thickness (θ), and shape factor ($H = \delta^*/\theta$) measured for the flat plate with and without the porous inserts at U_∞ of 20 m/s are tabulated in Table III. The results are only presented for some selected boundary layer locations for the sake of brevity. Results show that in the case of less permeable surfaces (80 PPI and 45 PPI), the boundary layer thickness, displacement thickness, and momentum thickness increase compared to the baseline case (solid surface) at each measurement locations. In the case of the highly permeable surface (25 PPI surface), results show that the boundary layer displacement thickness and momentum thickness increase compared to the solid case, however, show a reduction compared to the 80 PPI and 45 PPI surfaces. The boundary layer thickness for the 25 PPI surface is found to be the lowest compared to the other cases, which is believed to be due to the material being very permeable and that the boundary layer is more able to penetrate and sink into the porous media, which causes a reduction in the boundary layer thickness.

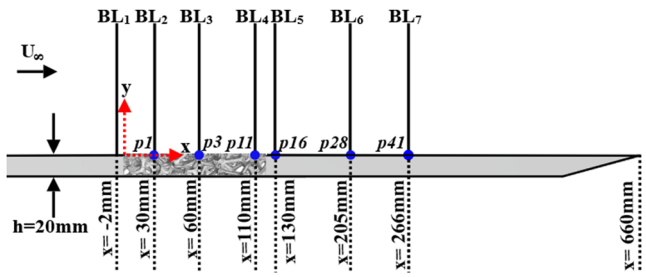

FIG. 5. The schematic of the flat plate and the position of the hot-wire for boundary layer (BL_i) measurements.

TABLE III. Boundary layer thickness (δ), displacement thickness (δ^*), momentum thickness (θ), and shape factor (H) for the flat plate with and without the porous inserts at U_∞ of 20 m/s before the test-section (BL_1), over the test-section (BL_3 and BL_4), and after the test-section (BL_5 and BL_7).

		BL_3				BL_4				BL_5				BL_7			
	BL_1	Solid	80 PPI	45 PPI	25 PPI	Solid	80 PPI	45 PPI	25 PPI	Solid	80 PPI	45 PPI	25 PPI	Solid	80 PPI	45 PPI	25 PPI
δ (mm)	25.4	26.9	32.5	35.8	30.7	30.0	30.8	32.5	28.3	31.1	31.7	33.2	29.1	33.9	37.3	36.9	36.1
δ^* (mm)	3.8	3.8	5.3	5.5	5.0	4.0	5.1	6.0	5.0	4.0	5.7	5.3	5.4	4.0	6.1	6.1	6.2
θ (mm)	2.9	3.0	3.9	3.9	3.7	3.2	3.6	4.3	3.5	3.2	4.0	3.7	3.7	3.2	4.4	4.3	4.4
H	1.3	1.3	1.4	1.4	1.4	1.3	1.4	1.4	1.4	1.3	1.4	1.4	1.4	1.3	1.4	1.4	1.4

The measurements were conducted at the free-stream velocity of $U_\infty = 20$ m/s, corresponding to the Reynolds number of $Re_{BL_1} = 3.6 \times 10^4$. A single wire probe was used, and the data had been collected with a very fine spatial resolution between $y \approx 0$ mm and 120 mm. The measurements were taken over the whole test section area ($x = 30$ mm, 60 mm, and 110 mm) and at the region upstream ($x = -2$ mm) and downstream ($x = 130$ mm, 205 mm, and 266 mm) of the surface treatment section to obtain a full picture of the boundary layer behavior. The y-axis of the boundary layer profiles was normalized by the boundary layer thickness at BL_1, $x = -2$ mm (before the test section), upstream of the test section area. This is because, at BL_1, the fluid velocity in the x-direction approaches zero when the fluid is in direct contact with the solid boundary, bringing about no-slip condition. This will not be the same in the case of the porous boundary, which involves the penetration of flow into the porous medium.[46] As expected, the mean velocity profiles at BL_1, upstream of the test section, are found to be similar for all cases and are therefore not presented here. For the solid wall, the turbulent boundary layer growth observed is almost similar in all the measurement locations, while a distinct growth of the boundary layer profiles is observed in the case of the porous walls, downstream of BL_1 for all the porous cases, except for the highly permeable surface (25 PPI material). The different behavior of the 25 PPI case can also be related to the flow penetration effects. The difference between the highly permeable surface (25 PPI) with the other cases will be further discussed in Secs. IV–VII.

The normalized rms of the fluctuating flow velocity, on the other hand, clearly shows that the whole energy cascade of the boundary layer changes significantly as a result of the flow interaction with the porous surfaces. The rms velocity results for the solid wall show a lower level of velocity fluctuations compared to that of the porous cases at the near-the-wall locations and then gradually decrease to the rms velocity of the free-stream flow away from the surface. By contrast, the rms velocity results for the porous cases, especially for the highly permeable materials at BL_3 ($x/\delta_{BL_1} = 2.4$) and BL_4 ($x/\delta_{BL_1} = 4.4$) (over the porous section) and at BL_5 ($x/\delta_{BL_1} = 5.2$), BL_6 ($x/\delta_{BL_1} = 8.2$), and BL_7 ($x/\delta_{BL_1} = 10.6$) (downstream of the porous section), revealed drastically different boundary layer behavior. A significant increase in the rms velocity magnitude and the emergence of the peak velocities ($y/\delta_{BL_1} \approx 0.05$–$0.5$) can be seen in the near the wall region of the plate, as the flow travels over the porous region (BL_3 and BL_4). The peak of the rms velocities, however, diminishes slowly, and the peaks flatten downstream of the porous surface (BL_6 and BL_7), peaking at around $y/\delta_{BL_1} \approx 0.5$. It can also be seen that the near-the-wall turbulent energy content increases in the normal direction from the wall and subsequently reduces to the standard boundary layer form (solid surface) at $y/\delta_{BL_1} > 1$. The increase in the energy content of the velocity fluctuations in the vicinity of the porous surface had the effect of increasing the flow shear stress, which can be attributed to the frictional forces due to the rough surface of the material. This is consistent with the surface roughness results obtained in Fig. 3(b).

A. Velocity power spectra in the boundary layer

Figure 6 shows the velocity power spectral density (PSD) as a function of frequency within the boundary layer at different axial locations over the porous surface at BL_3 ($x/\delta_{BL_1} = 2.4$) and BL_4 ($x/\delta_{BL_1} = 4.4$) and after the porous surface at BL_5 ($x/\delta_{BL_1} = 5.2$) and BL_7 ($x/\delta_{BL_1} = 10.6$). In order to obtain the energy frequency spectra at different boundary layer locations, the Welch power spectral density[47] with a Hamming window function was performed on the time-domain data for segments of equal length with 50% overlap. The number of segments is chosen such that it provides us with a frequency resolution of 32 Hz. The velocity fluctuation energy power spectrum is taken at (a) a point near the surface ($y/\delta_{BL_1} = 0.02$), (b) at the locations further away from the plate surface ($y/\delta_{BL_1} = 0.5$), and (c) at $y/\delta_{BL_1} = 0.75$. Results have clearly shown that the porous wall causes an increase in the flow energy content near the surface ($y/\delta_{BL_1} = 0.02$) over the whole frequency range, except at high frequencies, the energy spectra are very similar to that of the solid wall. The largest increase in the energy content near the surface can be seen for the higher permeability surface treatment. This is believed to be due to the frictional forces acting on the flow due to the porous surface, which is in agreement with the rms velocity results shown in Fig. 4. It is also seen that the frictional forces reduce slowly at the downstream locations and after the porous surface region. The results also show that the overall energy content of the larger turbulence structures associated with the porous surface at about 50% and 75% of the boundary layer thickness are reduced significantly and match the results of the solid surface. These reductions in the energy content can be interpreted as a cascade process that takes place at different layers of the boundary layer, where the energy due to the frictional forces or any related sources (i.e., internal hydrodynamic field inside the porous medium) increases at the near-the-wall

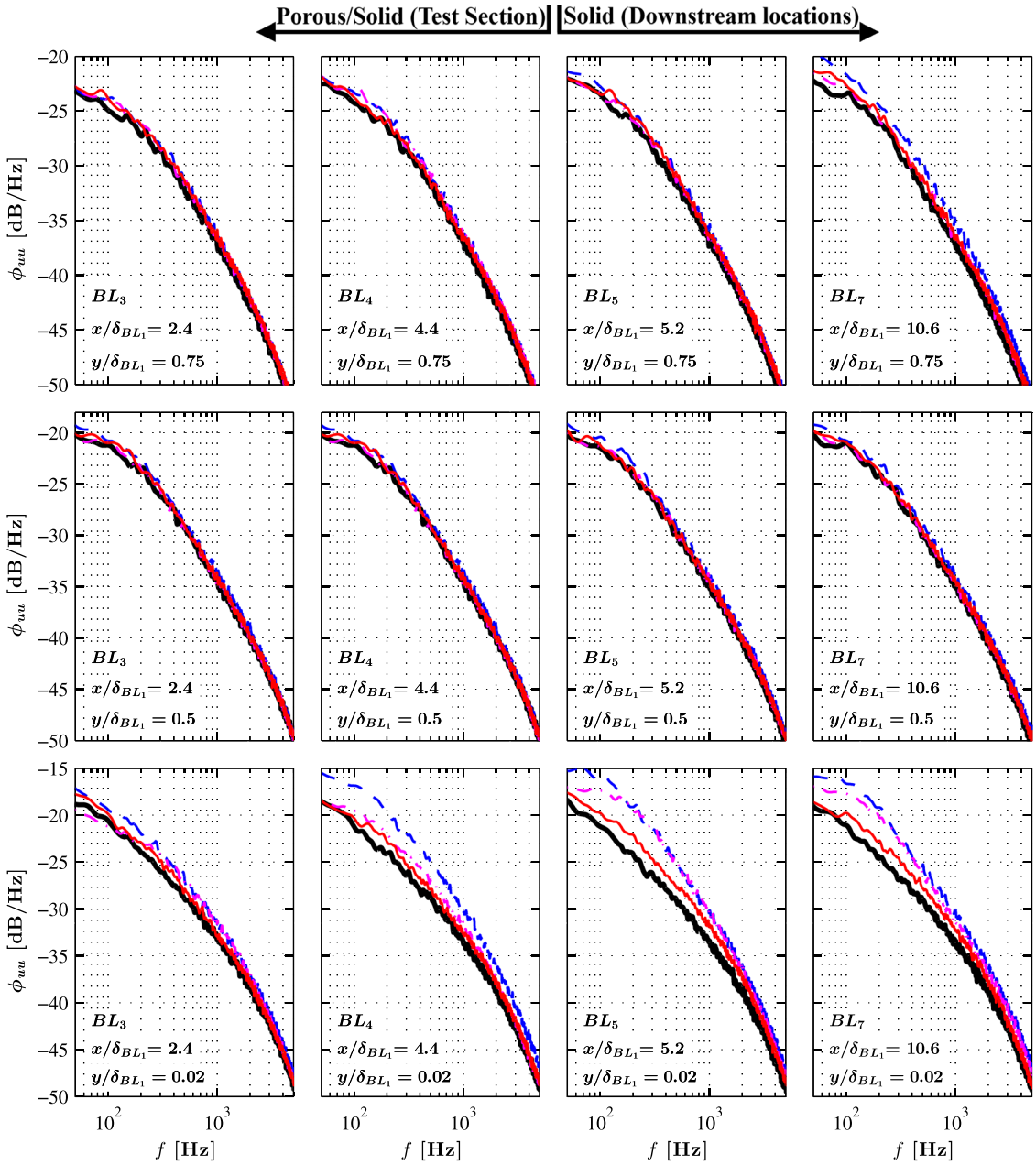

FIG. 6. Power spectra of the velocity within the boundary layer [ϕ_{uu} (dB/Hz)].

locations but then reduces shortly at locations above the surface (y/δ_{BL_1} = 0.5 and 0.75), over, and after the porous section.

IV. WALL PRESSURE POWER SPECTRA

To gain an insight into the effects of the porous surface on the boundary layer and surface pressure fluctuations exerted on the surface due to the boundary layer, a series of unsteady pressure measurements have been carried out over and after the porous section. Figure 7 presents the point spectra of the surface pressure fluctuations $\phi_{pp}(f)$, obtained from the transducers located over the porous section [$p3$ (x/δ_{BL_1} = 2.4) and $p11$ (x/δ_{BL_1} = 4.4)] and downstream of the porous section [$p16$ (x/δ_{BL_1} = 5.2) and $p41$ (x/δ_{BL_1} = 10.6)]. The locations of the transducers are shown in Fig. 1(a). It has been observed that the use of a porous surface increases the broadband energy content of the pressure fluctuations over the whole frequency range over the porous surface ($p3$ and $p11$). Also, the emergence of a small broadband hump between f = 100 and 400 Hz can be seen at the locations over the porous surface ($p3$ and $p11$) and downstream of the porous surface ($p16$), especially for the porous samples with high permeability (25 and 45 PPI). This broadband hump, however, dissipates very quickly at the further downstream locations, after the test section ($p41$). The increase in the broadband energy content and the development of a broadband hump can be due to either (a) the frictional forces between the rough porous surface and the flow or (b) the existence of a localized strong hydrodynamic field inside the porous medium. This will be further discussed in Sec. IV A. The results have also shown a reduction of ϕ_{pp} over the high frequency range, f > 7000 Hz, at the locations downstream

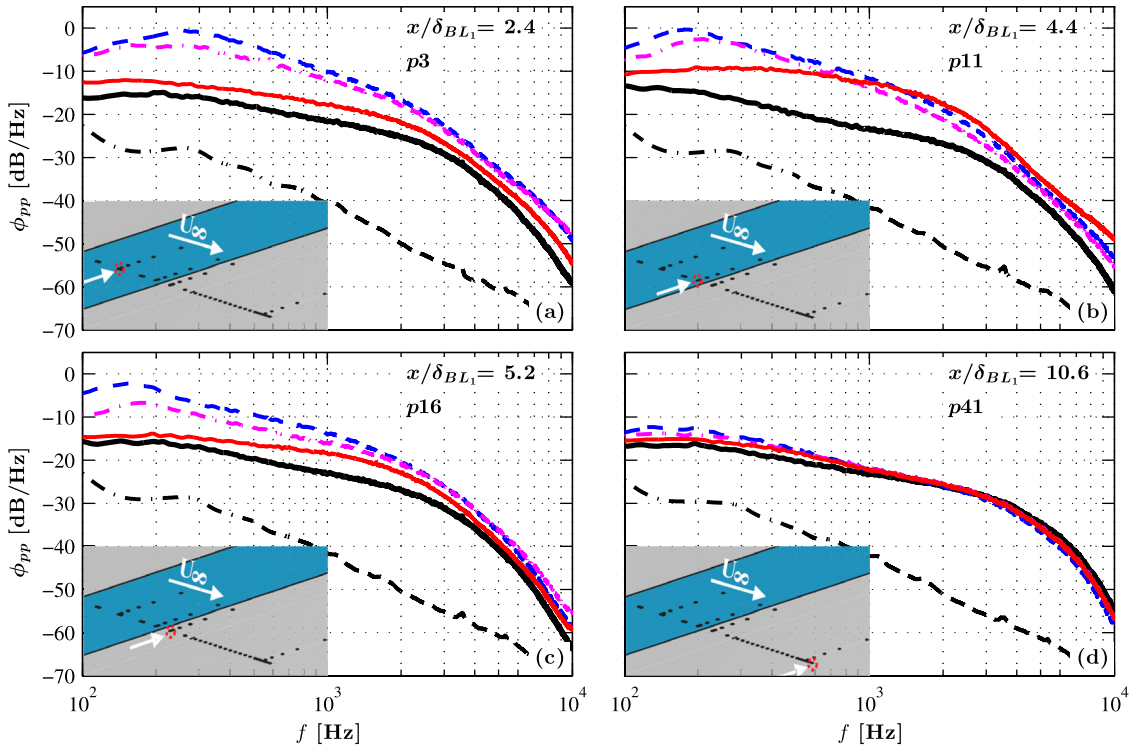

FIG. 7. Point spectra of pressure fluctuations at different streamwise locations over and after the porous surface. *Solid* (black solid curve), *porous* 80 *PPI* (red solid curve), *porous* 45 *PPI* (pink dotted-dashed curve), *porous* 25 *PPI* (blue short-dashed curve), and *background noise* (black dotted-dashed curve).

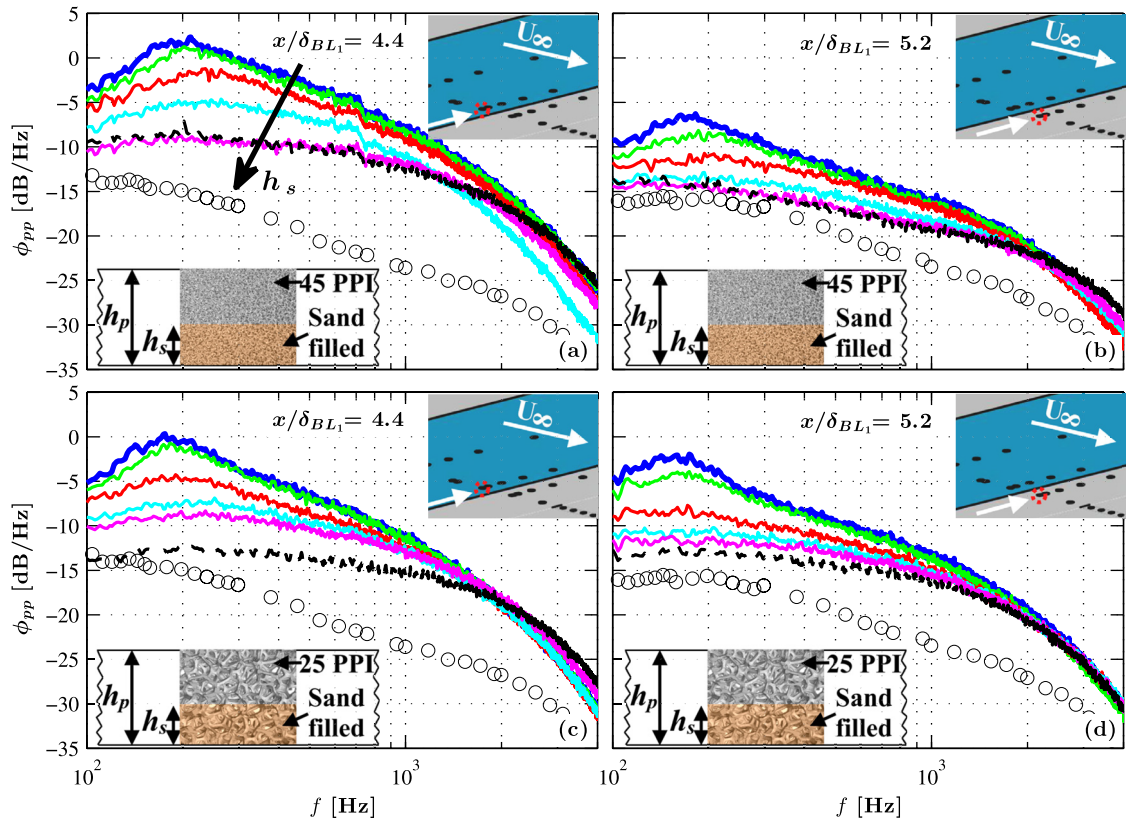

FIG. 8. Power spectral density of pressure measured by transducers $p11$ and $p16$ with different thickness of porous 45 and 25 PPI filled with sand. *Solid surface* (circles), $h_s/h = 1.0$ (black solid curve), $h_s/h = 0.9$ (pink solid curve), $h_s/h = 0.75$ (blue solid curve), $h_s/h = 0.5$ (red solid curve), $h_s/h = 0.5$ (green solid curve), and $h_s/h = 0$ (violet solid curve).

of the porous section ($p41$), i.e., $5.4\delta_{BL_1}$ after the porous section.

A. On the source of the broadband hump

As discussed in Sec. IV, the increase in the velocity energy content in the near-the-wall region can be attributed to the frictional forces acting on the porous materials. However, the emergence of a broadband hump, observed in Fig. 7 between $f \approx 100$ and 400 Hz, can only be seen in the case of highly permeable samples (25 PPI and 45 PPI) and dissipates quickly with distance from the plate. In order to examine the effect of the surface frictional forces and the existence of the internal hydrodynamic field, the porous section was filled with a fine grain sand, with a diameter of approximately 0.125 mm–0.25 mm[48] at different heights (h_s), as shown in Fig. 8. The porous surface roughness effect has been investigated by filling the porous 45 PPI and 25 PPI material with different sand heights (h_s/h), namely, $h_s/h = 0$ (fully permeable), $h_s/h = 0.25$, $h_s/h = 0.5$, $h_s/h = 0.75$, $h_s/h = 0.9$, and $h_s/h = 1.0$ (fully blocked but with a rough surface). The surface pressure PSD results are presented for two locations $x/\delta_{BL_1} = 4.4$ ($p11$) and $x/\delta_{BL_1} = 5.2$ ($p16$), i.e., over the porous surface and downstream of the porous section, respectively.

Figure 8 shows that the broadband hump at $f \approx 200$ only appears for the porous medium configurations with fully permeable ($h_s/h = 0$ sand) and slightly filled up ($h_s/h = 0.25$ and 0.5 sand) cases. Results also show that the broadband hump disappears gradually with increasing the sand height (h_s) in the porous medium, in which case there is not enough space available for the development of the internal hydrodynamic field. The results, therefore, confirm that the broadband hump observed at $f \approx 200$ cannot be due to the surface roughness effects. Hence, as expected, the emergence of the broadband hump can only be due to the existence of the hydrodynamic field and the flow recirculation inside the high permeability porous inserts.

V. FLOW VELOCITY AND PRESSURE CORRELATION ANALYSIS

In this section, further investigation on the changes in the boundary layer turbulent flow structures will be conducted by studying the coherence and correlation of the boundary layer velocity and the surface pressure signals over the porous and solid surfaces.

A. Surface pressure spanwise coherence and coherence length

In order to understand and decipher information related to the changes to the flow structures associated with rough-permeable surfaces, it is of significant importance to analyze the stochastic characteristics of the turbulent coherent structures over the porous wall. To understand these effects, the spanwise coherence of the turbulent structures and their corresponding spanwise coherence length using the pressure transducers ($p3$-$p7$, $p11$-$p15$, $p16$-$p20$, and $p35$-$p39$), distributed along the span at $x/\delta_{BL_1} = 2.4$ (middle of the porous section), $x/\delta_{BL_1} = 4.4$ (end of the porous section), $x/\delta_{BL_1} = 5.2$, and $x/\delta_{BL_1} = 10.2$, are studied. The coherence ($\gamma^2_{p'_i p'_j}$) and the spanwise coherence length (Λ_p) between the spanwise transducers are calculated using Eqs. (1) and (2), respectively, as

$$\gamma^2_{p'_i p'_j}(f, \xi_z) = \frac{|\Phi(f, p'_i, p'_j)|^2}{|\Phi(f, p'_i, p'_i)||\Phi(f, p'_j, p'_j)|} \tag{1}$$

and

$$\Lambda_p(f) = \int_0^\infty \gamma_{p'_i p'_j}(f, \xi_z) d\xi_z, \tag{2}$$

where $0 \le \gamma^2_{p'_i p'_j} \le 1$, $\Phi(f, p'_i, p'_j)$ denotes the cross-power spectral density between two pressure signals, and ξ_z denotes the pressure transducers separation distance in the z-direction. The results are presented only when the pressure signal is at least 10 dB higher than the background noise.

Figure 9 shows the spanwise coherence ($\gamma^2_{p'_i p'_j}$) as a function of the frequency (f), measured along the span for a wide range of spanwise spacings $0 < \xi_z/\delta_{BL_1} < 1.7$ for the solid (baseline) and porous (80, 45, and 25 PPI) cases. In the case of the solid surface, as anticipated, a strong coherence can be seen in the frequency region up to ≈400 Hz between the pressure signals at all the span locations. The results for the porous surfaces, on the other hand, clearly show that the porous treatment has a strong impact on the spanwise coherence of the flow structures, especially over the test section region. In the case of the porous 80 PPI surface, the spanwise turbulent structure decays quickly with ξ_z over the whole frequency range at $x/\delta_{BL_1} = 2.4$ and $x/\delta_{BL_1} = 4.4$. Immediately downstream of the test section ($x/\delta_{BL_1} = 5.2$ and $x/\delta_{BL_1} = 10.2$), the coherence behavior for the 80 PPI case changes completely, with the $\gamma^2_{p'_i p'_j}$ of the flow structures increasing significantly, almost twice larger than the results obtained at $x/\delta_{BL_1} = 2.4$. By contrast, the 45 PPI and 25 PPI samples exhibit much lower coherence values compared to that of the solid case, over the porous region ($x/\delta_{BL_1} = 2.4$ and $x/\delta_{BL_1} = 4.4$). However, similar to the findings in Fig. 7, the emergence of a broadband peak can be seen at the same frequency region between $f = 100$ and 400 Hz (shaded region) for the smaller transducers spacing distances, ξ_z of 0.13 δ_{BL_1} and 0.45 δ_{BL_1}. As discussed in Sec. IV A, this phenomenon is believed to be due to the emergence of a strong hydrodynamic field inside the porous medium. This broadband hump is also seen in the immediate locations after the test section ($x/\delta_{BL_1} = 5.2$) for both the 45 PPI and 25 PPI materials, but dissipating rapidly at the further downstream locations. At $x/\delta_{BL_1} = 10.2$, the $\gamma^2_{p'_i p'_j}$ of the boundary layer flow structures begin to behave very similar to that of the solid surface [Fig. 9(m)], indicating the redevelopment of the boundary layer coherent structures.

Figure 10 shows the effect of the porous surface on the spanwise correlation length (Λ_p) calculated using Eq. (2), based on the coherence of the pressure fluctuations collected using the spanwise transducers. The thick black line shows the spanwise correlation length for the baseline (solid) case. As expected, the spanwise correlation length remains very similar for the baseline case over $x/\delta_{BL_1} = 2.4$–10.2, which is consistent with the results observed in Figs. 6, 7, and 9. For the porous 80 PPI case, the correlation length is found to be much lower than the baseline case over the whole frequency

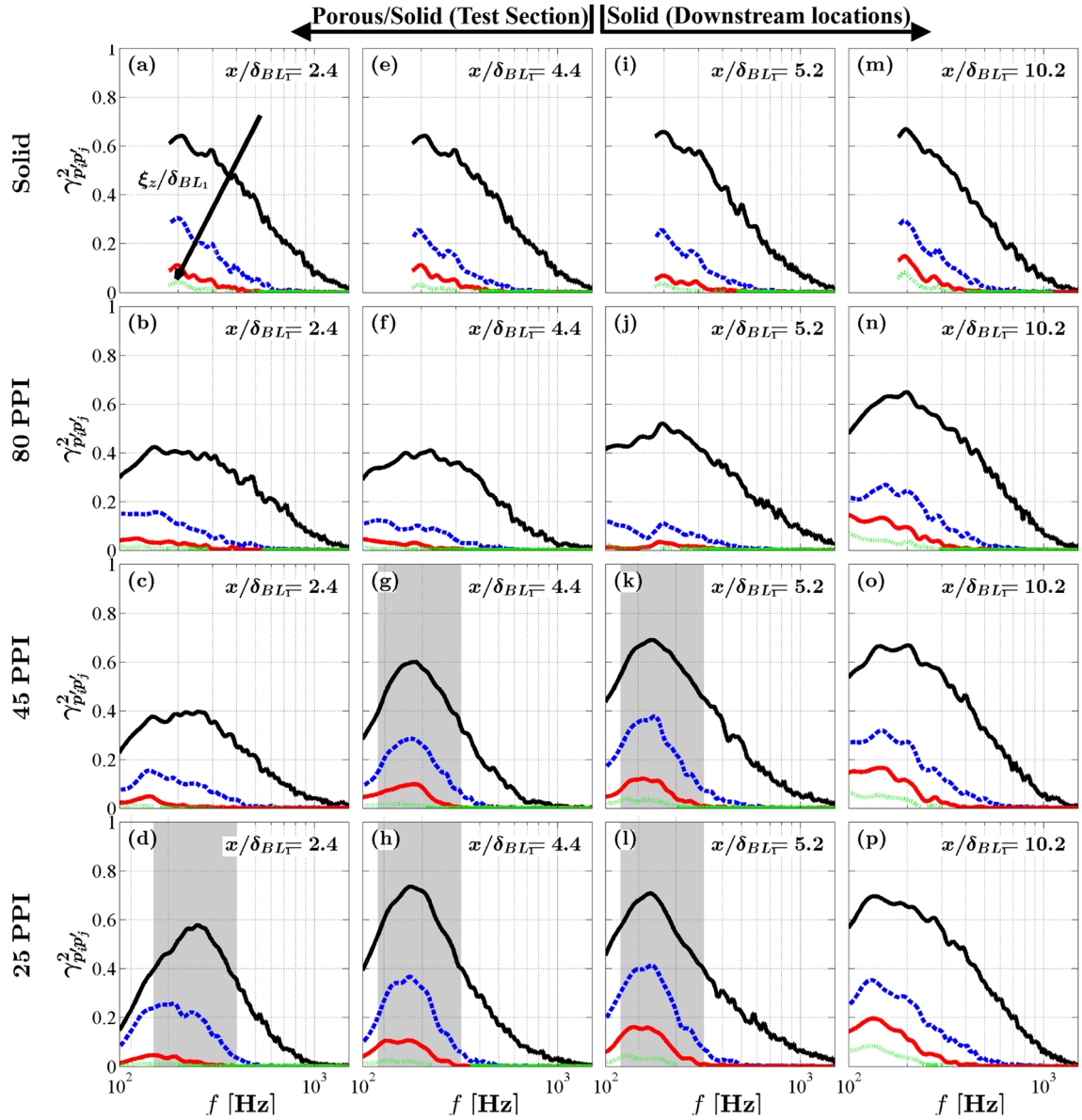

FIG. 9. Spanwise coherence between spanwise transducers at $x/\delta_{BL_1} = 2.4$ [(a)–(d)], $x/\delta_{BL_1} = 4.4$ [(e)–(h)], $x/\delta_{BL_1} = 5.2$ [(i)–(l)], and $x/\delta_{BL_1} = 10.2$ [(m)–(p)]. $\xi_z/\delta_{BL_1} = 0.13$ (black solid curve), $\xi_z/\delta_{BL_1} = 0.45$ (blue short-dashed curve), $\xi_z/\delta_{BL_1} = 0.96$ (red solid curve), and $\xi_z/\delta_{BL_1} = 1.68$ (green dotted curve). *The shaded areas signify the broadband hump observed in* Fig. 7.

range (100 Hz $\lesssim f \lesssim$ 700 Hz) for the locations over and immediately after the porous section, consistent with the results in Fig. 9. The spanwise coherence length results in the case of the porous 45 PPI and 25 PPI surfaces show a higher broadband hump than that of the solid case in the low frequency range ($\lesssim$200 Hz), which is also in agreement with the observations in Figs. 7–9. It is observed that the spanwise length scales for both the porous cases increase after the porous section and become very similar to the solid case at $x/\delta_{BL_1} = 10.2$. This is to say that the effects of a porous surface on the large coherent structures seem to have faded away $5\delta_{BL_1}$ after the porous section. It is clear that the porous surface treatment significantly changes the coherence and spanwise coherence length of the surface pressure fluctuations at the low frequency range and completely eliminates the pressure fluctuations at a high frequency range, especially for the 25 PPI treated surface case.

B. Surface pressure spatio-temporal correlation analysis

The spatial and temporal characteristics of the boundary layer structures can be studied from the space-time correlation of the wall pressure fluctuations, defined as

$$R_{p'_i p'_j}(\xi_x, \tau) = \frac{\overline{p'_i(x_i + \xi_x, t + \tau) p'_j(x_j, t)}}{p'_{i_{rms}}(x_i) p'_{j_{rms}}(x_j)}, \tag{3}$$

where p'_i is the wall pressure signal collected from the pressure transducer at the location (x_i, y_i), $p'_{i_{rms}}$ is the root-mean-square of p'_i, τ denotes the time-delay between the pressure signals, ξ_x is the distance between the transducers in the x-direction, and the overbar represents the time averaging. Equation (3) reduces to the temporal autocorrelation, $R_{p'_i p'_i}(\tau)$, when $\xi_x = 0$.

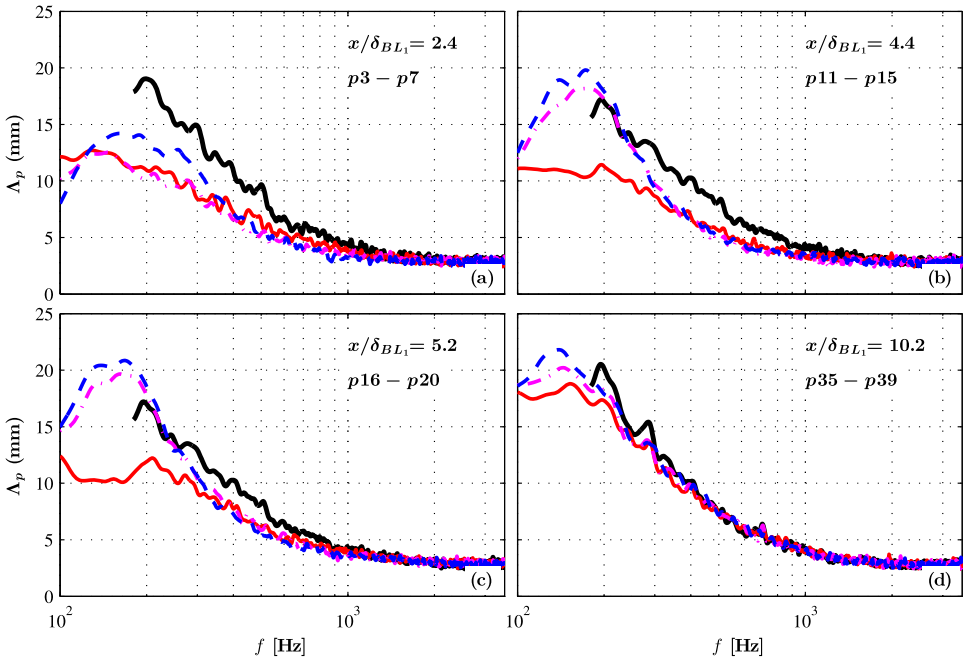

FIG. 10. Spanwise coherence length at (a) x/δ_{BL_1} = 2.4, (b) x/δ_{BL_1} = 4.4, (c) x/δ_{BL_1} = 5.2, and (d) x/δ_{BL_1} = 10.2. *Solid* (black solid curve), *porous* 80 *PPI* (red solid curve), *porous* 45 *PPI* (pink dotted-dashed curve), and *porous* 25 *PPI* (blue short-dashed curve).

1. Autocorrelation

The temporal correlation scale is the time taken for the cross-correlation ($R_{p_i'p_i'}(\tau)$) to reach zero, i.e., where maximum width of the autocorrelation coefficient is observed, along the time-axis. Figure 11 shows the temporal autocorrelations of the surface pressure fluctuations, $R_{p_i'p_i'}(\tau)$, for transducers at different axial locations over the porous surface [$p1$ (x/δ_{BL_1} = 1.2) and $p11$ (x/δ_{BL_1} = 4.4)] and after the porous surface [$p16$ (x/δ_{BL_1} = 5.2) and $p41$ (x/δ_{BL_1} = 10.6)]. The presented data are plotted against the normalized time-delay $\tau U_\infty/\delta_{BL_1}$.

The $R_{p_i'p_i'}(\tau)$ results for the solid surface condition show the largest width of the autocorrelation coefficient at τ^* = 0 among all the tested cases and that no regions of negative correlations can be seen, indicating the presence of large-scale turbulence structures in the pressure field. The results also show that the autocorrelation signal width increases by

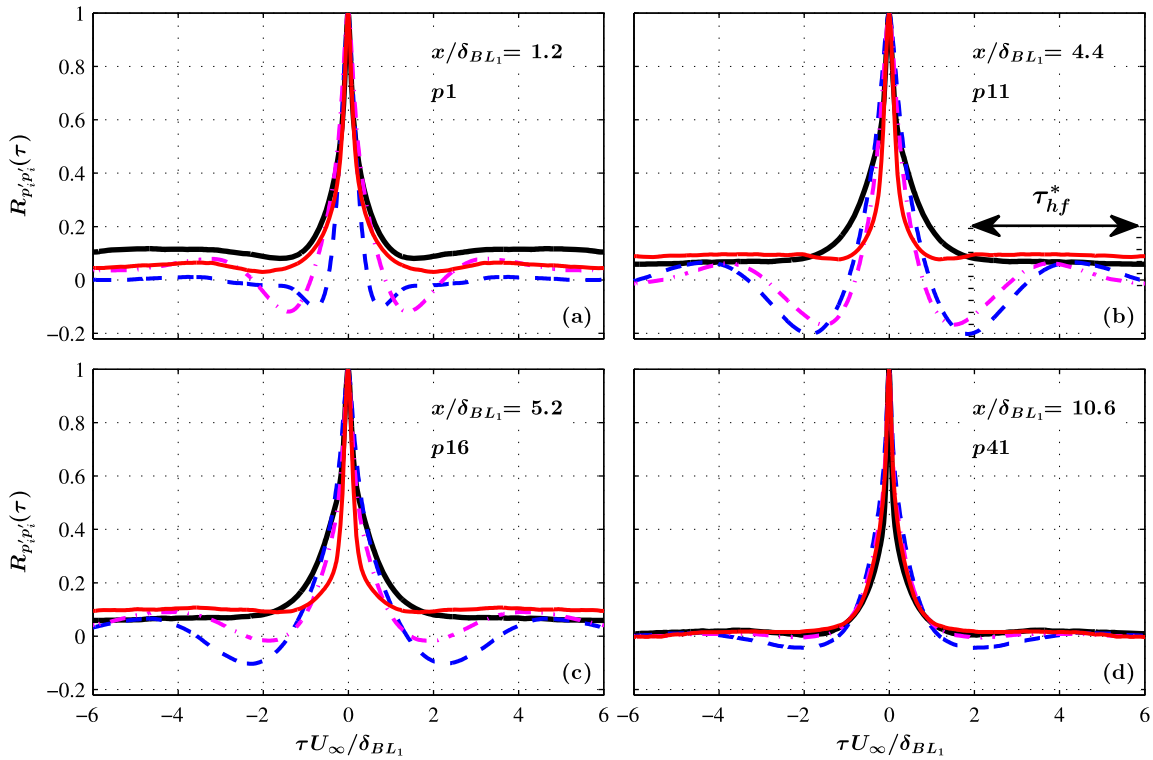

FIG. 11. Autocorrelation of the wall pressure fluctuations as a function of $\tau^* = \tau\ U_\infty/\delta_{BL_1}$. *Solid* (black solid curve), *porous* 80 *PPI* (red solid curve), *porous* 45 *PPI* (pink dotted-dashed curve), and *porous* 25 *PPI* (blue short-dashed curve).

moving in the downstream direction (+x) due to the development of the turbulence boundary layer and the thickening of the boundary layer. In general, the autocorrelation results for the porous cases change significantly over $p1$ and $p11$, and after the porous section ($p16$) and become almost identical to that of the baseline case (solid surface) at further downstream location ($p41$), i.e., $5.4\delta_{BL_1}$ away from the porous section. For the porous 80 PPI case, it can be seen that the autocorrelation width at $\tau U_\infty/\delta_{BL_1} = 0$ is narrower compared to the solid case, indicating a reduction in the temporal scales of the boundary layer structures. The results have also shown that there is a significant change in the nature of the correlation, where a sharp decay in the correlation occurs at $\tau U_\infty/\delta_{BL_1} = 0$ for all the measurement locations over the porous surface, which is believed to be due to the pressure exerted by the downstream moving boundary layer turbulence structure at the transducer location. The autocorrelation curves for the 45 PPI and 25 PPI surfaces, on the other hand, show a much faster decay at $\tau U_\infty/\delta_{BL_1} = 0$ and therefore much narrower band than the other two cases, particularly for the 25 PPI surface at $p1$ ($x/\delta_{BL_1} = 1.2$), signifying a greater reduction in the temporal scales of the boundary layer structures. In the case of highly permeable porous surfaces (45 PPI and 25 PPI), the sharp decay in the autocorrelation is followed by an area of negative correlation and semi-periodic oscillation. Unlike the solid and porous 80 PPI surfaces, the results indicate that two potential mechanisms can be involved in the abrupt changes in the autocorrelation profiles, namely, (a) the existence of quasi-periodic hydrodynamic field with the periodicity of τ^*_{hf} (i.e., $\tau^* = \tau U_\infty/\delta_{BL_1}$) and (b) a fast-decaying event at $\tau U_\infty/\delta_{BL_1} = 0$. As observed in Figs. 11(a) and 11(b) for the transducers located on the porous surface, the autocorrelation exhibits a fast decay at $\tau U_\infty/\delta_{BL_1} = 0$, similar to that of the 80 PPI material, which is due to the pressure signature of the downstream moving boundary layer structures. The autocorrelation result also shows a periodicity behavior that occurs within $1.5 < |\tau U_\infty/\delta_{BL_1}| < 5$, which corresponds to the broadband hump frequency observed in Fig. 7. This quasi-periodic structure, as discussed in Sec. IV A, is believed to be due to the internal hydrodynamic field inside the porous medium. The results also show that the spatially and temporally fast-decaying quasi-periodic hydrodynamic field in the case of 45 PPI and 25 PPI materials can only be seen within a certain axial distance from the porous section, of about $L_p = 40$ mm. The effect of porous section length on the formation of the internal hydrodynamic field will be further studied in Sec. VI.

Figure 12 shows the space-time correlations results obtained from the cross-correlation between the reference transducer downstream of the porous section ($p41$) and the upstream pressure transducers positioned along the mid-chord line. Results are presented for the separation distances ξ_x/δ_{BL_1} of about 0.16–9.44. The left column plots [(a), (c), (e), and (g)] show the correlation between all the streamwise transducers, where the black line ($\xi_x/\delta_{BL_1} = 0$) represents the autocorrelation information of the transducer $p41$ as the reference probe, while the different shades of gray curves show the cross-correlation between the reference probe and the upstream probes for all the investigated cases. The right column plots [(b), (d), (f), and (h)] show the space-time correlation contour plots, where the results are plotted over the two surface areas, i.e., over and after the porous surface. The dashed line represents the interface between the porous and solid surfaces (x = 120 mm). An envelope trend can be clearly seen from the cross-correlation periodicity and the amplitude variations for all the cases considered in this study. The cross-correlation $R_{p'_ip'_j}(\xi_x, \tau)$ results for the solid case show that the surface pressure correlations peak at positive time-delays, i.e., $\tau U_\infty/\delta_{BL_1} \geqslant 0$, indicating the presence of a downstream-moving hydrodynamic field, travelling in the direction of the free-stream flow. The results for the solid surface in Fig. 12(a) show that the correlation peaks shift very quickly in the positive time-delay direction, which indicates the existence of a long-lasting energy field [$R_{p'_ip'_j}$ drop to 0.1 within 10 non-dimensional time ($\tau U_\infty/\delta_{BL_1}$)] in the pressure field over the flat plate. A similar but less distinct behavior can also be observed for the 80 PPI surface case. Finally, in the case of the 45 PPI and 25 PPI surfaces, the $R_{p'_ip'_j}(\xi_x, \tau)$ results show that the surface pressure fluctuations have slightly higher correlation and that the correlation peaks shift slowly (larger time delay) at $\tau U_\infty/\delta_{BL_1} \geq 0$ compared to the solid case, which suggests that the turbulent structures convected in the downstream direction are primarily dominated by a short-lived energy field {$R_{p'_ip'_j}$ drop to 0.1 within $\tau U_\infty/\delta_{BL_1} \approx 5$ [Figs. 12(e) and 12(g)]} in the pressure field over the plate. The results in Fig. 12 show that as the separation distance (ξ_x) between the pressure probes increases, the time-delay of the maximum value in the cross-correlation (cross-correlation peak) increases. Hence, based on Taylor's frozen flow hypothesis, one can obtain the convection velocity, U_c, using the transducers distance and the maximum value of the cross-correlation time-delay ($[\tau\ U_\infty/\delta_{BL_1}]_{max}$) information, i.e., $U_c = (\xi_x/\delta_{BL_1})/[\tau\ U_\infty/\delta_{BL_1}]_{max}$.

The solid line in the contour plots (b), (d), (f), and (h), passing through the correlation lobe at $\tau\ U_\infty/\delta_{BL_1} \approx 0$, whose slope indicates the averaged normalized convection velocities U_c/U_∞. Note that the U_c/U_∞ is only determined from the cross-correlation of the transducers located after the test section region. The non-dimensional convection velocities U_c/U_∞ obtained from the cross-correlation between the reference transducer $p41$ and the upstream transducers are found to be about 0.8632, 0.8402, 0.7471, and 0.7135 for the solid, porous 80 PPI, porous 45 PPI, and porous 25 PPI cases, respectively. As expected, the flow over the solid surface has the highest convection velocity. By contrast, the convection velocity for the flow over the 25 PPI porous surface is the lowest. It can therefore be concluded that the porous surface can strongly reduce the convection velocity of the boundary layer structures.

C. Boundary layer velocity-pressure coherence analysis

The surface pressure and velocity fluctuation coherence studies at different locations within the boundary layer were conducted in order to characterize the spatial and temporal evolution of the coherent flow structures over the solid and porous surfaces and their role on the pressure field exerted

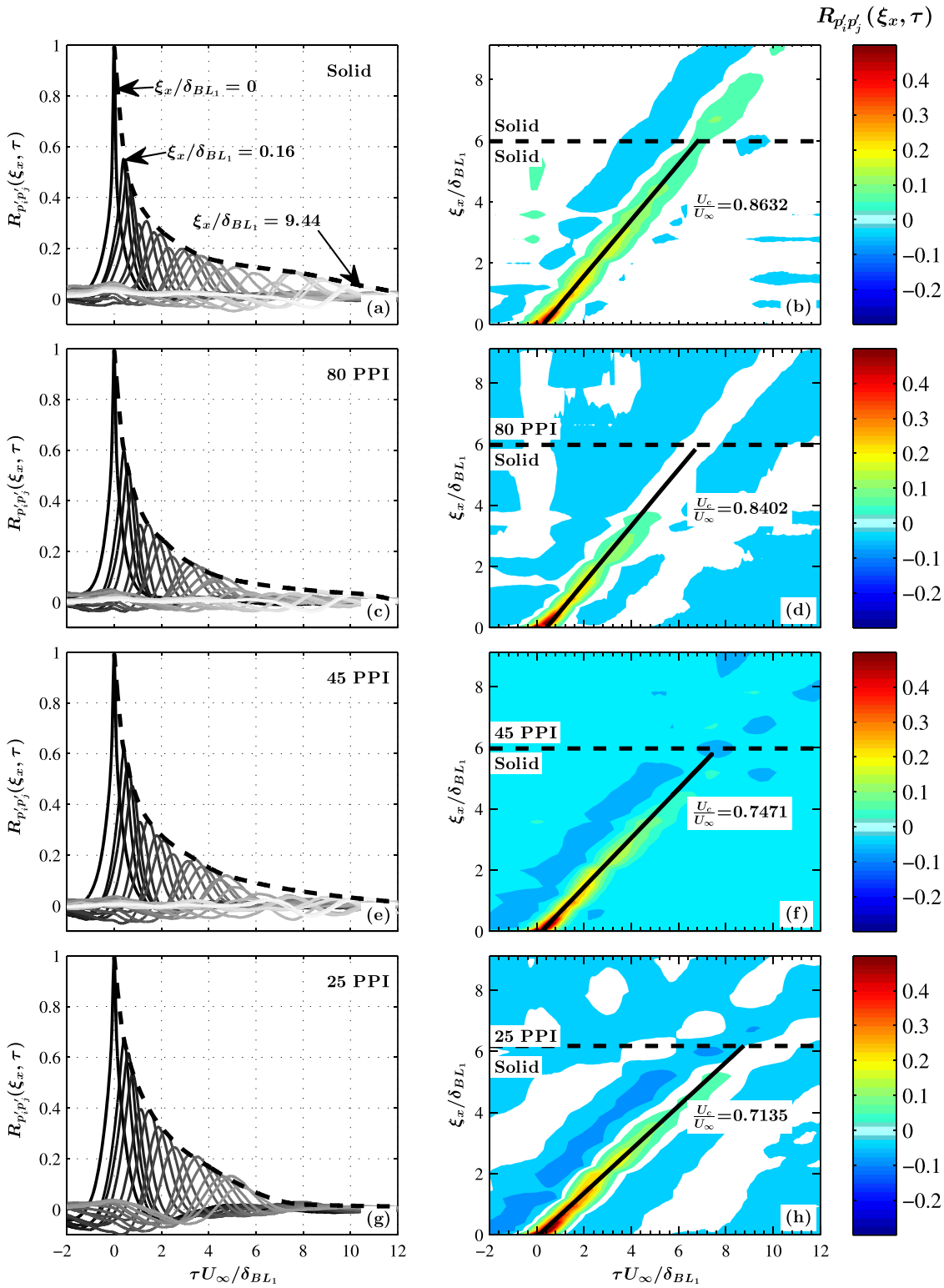

FIG. 12. Space-time correlations of wall pressure fluctuations between the streamwise transducers as a function of $\tau U_\infty/\delta_{BL_1}$ and the corresponding autocorrelation envelops shown by dashed lines.

on the surface. Simultaneous boundary layer flow velocity and surface pressure measurements were performed at four locations, namely, $p3$, $p11$, and $p16$ for the flow velocity of 20 m/s. A single wire probe was used, and the data had been collected between $y \approx 0$ mm and 120 mm normal to the wall at 63 locations above each transducer. To identify the pattern of the coherent turbulent structures in space, the coherence between the velocity and surface pressure signals is analyzed using Eq. (4) as

$$\gamma^2_{u'p'}(f,\xi_y) = \frac{|\Phi(f,u',p')|^2}{|\Phi(f,u',u')||\Phi(f,p',p')|}, \tag{4}$$

where $\Phi(f, u', p')$ denotes the cross-power spectral density function between the velocity and pressure signals and ξ_y is the distance of the hotwire probe from the surface.

Figure 13 presents the coherence between the flow velocity and the surface pressure fluctuations ($\gamma^2_{u'p'}$) measured at different distances, over the porous section [$p3$ ($x/\delta_{BL_1} = 2.4$) and $p11$ ($x/\delta_{BL_1} = 4.4$)] and downstream of the porous section [$p16$ ($x/\delta_{BL_1} = 5.2$) and $p41$ ($x/\delta_{BL_1} = 10.6$)]. The results for the solid surface case show a strong coherence in the low frequency region within about 30% of the boundary layer thickness ($0.05 \lesssim \xi_y/\delta_{BL_1} \lesssim 0.45$). The velocity-pressure coherence remains very similar for the solid case over all the locations measured ($x/\delta_{BL_1} = 2.4$–5.2), which is consistent with results observed in Figs. 6, 7, 9, and 10. The pressure-velocity coherence results for the case of porous surfaces are much more complex. The $\gamma^2_{u'p'}$ coherence results for the porous 80 PPI surface show a strong coherence trend at low frequencies, similar to that of the solid case, covering the boundary layer region of about $0.1 \lesssim \xi_y/\delta_{BL_1} \lesssim 0.65$, but with a much lower coherence intensity especially over the porous section ($p11$) and immediately downstream of the porous section ($p16$). The high coherence intensity area for the 80 PPI case is observed to have moved closer to the wall compared to that of the solid case, where the frictional forces are believed to dominate the velocity-pressure coherence, particularly at $x/\delta_{BL_1} = 2.4$. This high coherence peak is strongly suppressed at the downstream locations ($x/\delta_{BL_1} = 4.4$ and 5.2).

The friction-induced high coherence region observed at the near-the-wall locations is found to exist at all porous surface cases, particularly for the cases with high surface roughness (Ra), i.e., 45 PPI and 25 PPI surfaces. In the case of the porous 45 PPI surface, a pronounced velocity-pressure coherence reduction can be seen over the porous section ($p11$), covering the boundary layer region of about $0.1 \lesssim \xi_y/\delta_{BL_1} \lesssim 0.15$, which occurs only after a certain critical length of the porous surface. The results for the 25 PPI case, on the other hand, show a much weaker $\gamma^2_{u'p'}$ coherence, covering the boundary layer region of $\xi_y/\delta_{BL_1} \lesssim 0.1$, which is more confined to the near-the-wall area at $p3$, $p11$, and $p16$ compared to the 45 PPI case. It can also be seen that a broadband area of high velocity-pressure coherence appears between $f = 100$ and 400 Hz at $p3$ and $p11$ (over the porous surface), which overlaps the area of low frequency hump observed in the wall pressure spectra (Fig. 7). This broadband region is confined within a spatial domain over the porous surface and dissipates quickly at the downstream locations. As mentioned earlier, this is believed to be due to the emergence of a hydrodynamic field inside the porous medium, which takes place only in the case of highly permeable porous materials, i.e., 45 PPI and 25 PPI surfaces. As described earlier in Fig. 11, the emergence of this hydrodynamic field requires a long enough porous section

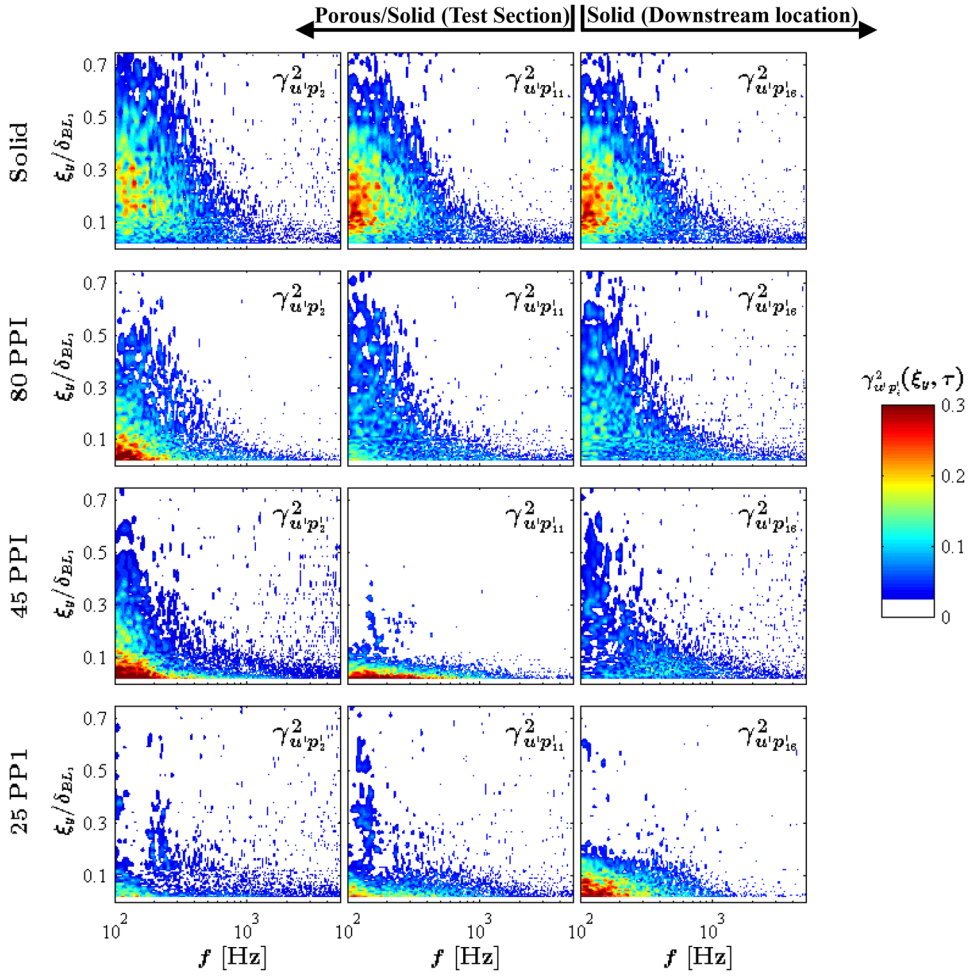

FIG. 13. Velocity-pressure coherence, $\gamma^2_{u'p'_i}$, at locations $p3$, $p11$, and $p16$ for solid, porous 80 PPI, porous 45 PPI, and porous 25 PPI surfaces.

to enable the flow penetration into the porous medium. The effects of the porous section length on the emergence of the internal hydrodynamic field will be shown and discussed in Sec. VI.

VI. FLOW PENETRATION CRITICAL LENGTH

The results in Secs. III and IV have shown that the use of a relatively high permeable substrate can lead to significant changes to the whole energy cascade of the boundary layer, reduction in the surface pressure fluctuations at high frequencies, and the emergence of a strong hydrodynamic field inside the porous medium. The velocity-pressure correlation and coherence analysis in Sec. V demonstrated that the coherence and the spanwise coherence lengths of the spanwise flow structures can be significantly reduced over the porous surface. The surface pressure spatio-temporal correlation analysis, on the other hand, showed that a quasi-periodic hydrodynamic field may emerge within porous media with high permeability and that the spanwise coherence length of the convected flow structures can reduce significantly. It is clear from the results that the boundary layer flow penetration into the porous medium has a strong influence on the above-mentioned effects. Hence, in order to allow a proper flow penetration, it is necessary for the flow to remain in contact with the porous medium over a long enough porous section. All the results presented previously were obtained for porous sections with a streamwise length of $L_p = 4.8\delta_{BL_1}$ (L_p = 120 mm). Further experiments have been conducted for the highly permeable porous materials (45 PPI and 25 PPI) with different streamwise lengths L_p with the incremental lengths of 5 mm (0.2 δ_{BL_1}), to investigate the effect of the porous section length on the above-mentioned phenomena. The shorter porous inserts are placed toward the end of the cavity section, while the upstream cavity between $x = 0$ and the porous section is filled with a solid plate of appropriate length and depth of 20 mm. For clarity, the length of the new porous sections is defined as L_{px} in this section. The results are only presented for some selected streamwise lengths, namely, L_{px}/δ_{BL_1} = 4.8 (120 mm), 3.2 (80 mm), 1.6 (40 mm), 0.8 (20 mm), and 0.6 (15 mm), for the sake of brevity.

The effect of the porous section length is analyzed using the power spectral density of the wall surface pressure results (ϕ_{pp}) at $x/\delta_{BL_1} = 4.4$ ($p11$) for the 45 PPI and 25 PPI materials, as presented in Fig. 14. Results are presented for five porous section lengths and also for the solid surface (circle marker). It is observed that the emergence of the localized broadband hump, previously shown in Figs. 7 and 11, is very sensitive to the length of the porous section. It can be seen clearly that the broadband hump emerges only for the porous sections with a streamwise length of $L_{px} \geqslant 1.6\delta_{BL_1}$. It is also apparent that the frequency associated with the broadband hump changes with the porous section length and that the localized broadband hump shifts to higher frequencies with decreasing the porous section length (L_{px}).

Finally, a thorough study on the surface pressure autocorrelation and the velocity-pressure coherence has been carried out to investigate and better understand the emergence of the internal hydrodynamic field and its relationship with the porous treatment length (L_{px}). The autocorrelation and the velocity-pressure coherence ($\gamma^2_{u'p'}$) results for the $p11$ transducer ($x/\delta_{BL_1} = 4.4$), where a significant effect on the boundary layer flow-porous interaction is observed, are shown in Figs. 15 and 16 for the 45 PPI and 25 PPI cases, respectively. Results are presented for different porous treatment lengths. The surface pressure autocorrelation results for the solid surface (circles) are also given for comparison. The autocorrelation results for all the porous surfaces confirm again that there exists a critical length for the emergence of the quasi-periodic hydrodynamic field within the porous medium. The quasi-periodic internal

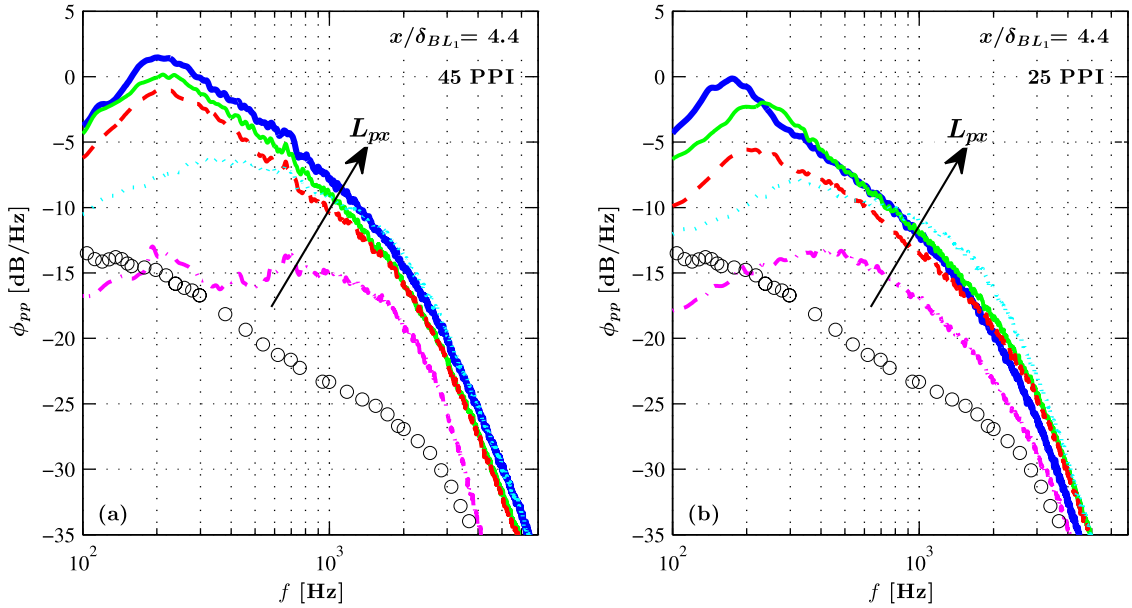

FIG. 14. Wall pressure fluctuations with different porous 45 PPI and 25 PPI lengths at x/δ_{BL_1} = 4.4 (p11). *Solid* (circle marker), L_{px}/δ_{BL_1} = 4.8 (blue solid curve), L_{px}/δ_{BL_1} = 3.2 (green solid curve), L_{px}/δ_{BL_1} = 1.6 (red short-dashed curve), L_{px}/δ_{BL_1} = 0.8 (blue dotted curve), and L_{px}/δ_{BL_1} = 0.6 (pink dotted-dashed curve).

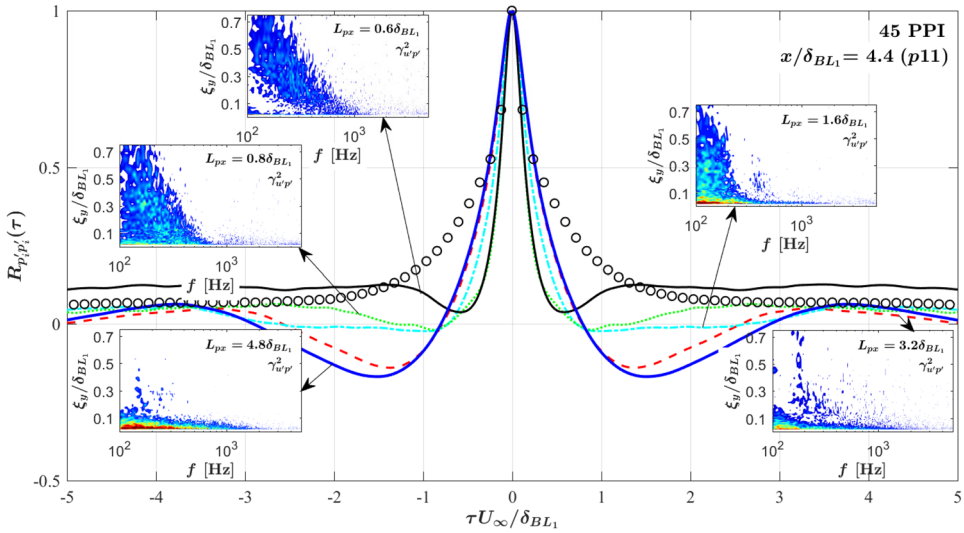

FIG. 15. Autocorrelation of the wall pressure fluctuations with different porous 45 PPI surface lengths and its velocity-pressure coherence ($\gamma^2_{u'p'}$) results at $x/\delta_{BL_1} = 4.4$ ($p11$).

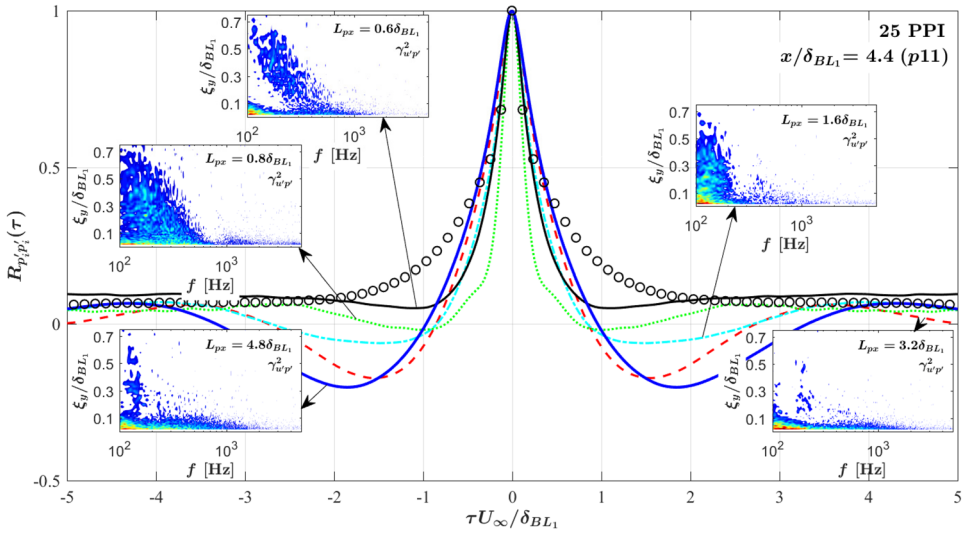

FIG. 16. Autocorrelation of the wall pressure fluctuations with different porous 25 PPI surface lengths and its velocity-pressure coherence ($\gamma^2_{u'p'}$) results at $x/\delta_{BL_1} = 4.4$ ($p11$).

hydrodynamic field for the long porous treatments for both the 45 PPI and 25 PPI cases, particularly for the cases with $L_{px}/\delta_{BL_1} > 1.6$, reveals itself as (a) a fast decaying oscillation within $1.5 < |\tau\ U_\infty/\delta_{BL_1}| < 5$ in the pressure autocorrelation results, in agreement with the results observed in Fig. 7, and (b) a high coherence broadband region near the surface in the pressure-velocity coherence results. The velocity-pressure coherence results also confirm the suppression of the coherent flow structures and the emergence of a broadband hump for the long porous surfaces.

VII. CONCLUSION

The use of porous treatments for flow control and suppression of aerodynamic noise at the source has been the subject of many studies in the past. With regard to the noise abatement applications, while most recent attention has focused on the reduction of the far-field noise from bluff-bodies and aerofoils using porous treatments, the near-field studies have shown that the changes to the boundary layer flow structures by the porous media are key to the success of the porous treatment as a passive method. This paper presents the results of an experimental investigation into the turbulent boundary layer flow interaction with a rough permeable wall on a long flat plate. Despite its simplicity, the experimental test-rig used in this study enables a large variety of different flow-porous interaction studies, such as the surface roughness, flow penetration, porous-flow viscous interaction, and hydrodynamic absorption effects of the porous media. Results have shown that the use of porous surface treatments leads to an increase in the energy content of the velocity fluctuations near the surface and a more rapid energy cascade within the boundary layer. The surface pressure PSD results have also shown that the porous surface treatment causes an increase in the overall pressure exerted on the surface. The near-field studies have shown that the penetration of the boundary layer flow into the highly permeable porous media can generate an internal hydrodynamic field, which can, in turn, reduce the frequency-energy content of the large boundary layer coherent structures and their spanwise correlation length. Results have also shown that a relatively long porous section is required to enable flow penetration inside the porous substrate. Moreover, it has been observed that

the existence of the quasi-periodic hydrodynamic field inside the porous medium and the reduction in the velocity-pressure coherence over the porous surface are inter-related and dependent on the effective length of the porous section. In addition to the direct application of the outcomes of this study to the field of aeroacoustics and development of bespoke aerodynamic-noise control techniques, the data can also be useful in other fields, such as aerodynamics of low drag surfaces, heat transfer of porous media, etc.

ACKNOWLEDGMENTS

The authors would like to acknowledge the financial support from Embraer S.A.

[1]B. Lyu, M. Azarpeyvand, and S. Sinayoko, "Prediction of noise from serrated trailing edges," J. Fluid Mech. **793**, 556–588 (2016).
[2]B. Lyu and M. Azarpeyvand, "On the noise prediction for serrated leading edges," J. Fluid Mech. **826**, 205–234 (2017).
[3]X. Liu, H. Kamliya Jawahar, M. Azarpeyvand, and R. Theunissen, "Aerodynamic performance and wake development of airfoils with serrated trailing-edges," AIAA J. **55**, 3669–3680 (2017).
[4]A. Afshari, M. Azarpeyvand, A. A. Dehghan, and M. Szoke, "Trailing edge noise reduction using novel surface treatments," AIAA 2016-2384, 2016.
[5]S. A. Showkat Ali, M. Azarpeyvand, and C. R. Ilario da Silva, "Experimental study of porous treatment for aerodynamic and aeroacoustic purposes," AIAA 2017-3358, 2017.
[6]S. A. Showkat Ali, X. Liu, and M. Azarpeyvand, "Bluff body flow and noise control using porous media," AIAA 2016-2754, 2016.
[7]H. Liu, M. Azarpeyvand, J. Wei, and Z. Qu, "Tandem cylinder aerodynamic sound control using porous coating," J. Sound Vib. **334**, 190–201 (2015).
[8]M. Szoke and M. Azarpeyvand, "Active flow control methods for the reduction of trailing edge noise," AIAA 2017-3004, 2017.
[9]S. Mahjoob and K. Vafai, "A synthesis of fluid and thermal transport models for metal foam heat exchangers," Int. J. Heat Mass Transfer **51**, 3701–3711 (2008).
[10]A. F. Zagni and K. V. Smith, "Channel flow over permeable beds of graded spheres," J. Hydraul. Div. **102**, 207–222 (1976).
[11]T. Geyer, E. Sarradj, and C. Fritzsche, "Porous airfoils: Noise reduction and boundary layer effects," Int. J. Aeroacoustics **9**, 787–820 (2010).
[12]J. Finnigan, "Turbulence in plant canopies," Annu. Rev. Fluid. Mech. **32**, 519–571 (2000).
[13]V. Prasad, "Flow instabilities and heat transfer in fluid overlying horizontal porous layers," Exp. Therm. Fluid Sci. **6**, 135–146 (1993).
[14]K. Suga, Y. Matsumura, Y. Ashitaka, S. Tominaga, and M. Kaneda, "Effects of wall permeability on turbulence," Int. J. Heat Fluid Flow **31**, 974–984 (2010).
[15]C. Manes, D. Poggi, and L. Ridolfi, "Turbulent boundary layers over permeable walls: Scaling and near-wall structure," J. Fluid Mech. **687**, 141–170 (2011).
[16]W. Breugem, B. Boersma, and R. Uittenbogaard, "The influence of wall permeability on turbulent channel flow," J. Fluid Mech. **562**, 35–72 (2006).
[17]F. Kong and J. Schetz, "Turbulent boundary layer over porous surfaces with different surface geometries," in 20th Aerospace Sciences Meeting, 1982.
[18]D. Poggi, A. Porporato, L. Ridolfi, J. Albertson, and G. Katul, "The effect of vegetation density on canopy sub-layer turbulence," Boundary-Layer Meteorol. **111**, 565–587 (2004).
[19]J. Jimenez, M. Uhlmann, A. Pinelli, and G. Kawahara, "Turbulent shear flow over active and passive porous surfaces," J. Fluid Mech. **442**, 89–117 (2001).
[20]M. E. Rosti, L. Cortelezzi, and M. Quadrio, "Direct numerical simulation of turbulent channel flow over porous walls," J. Fluid Mech. **784**, 396–442 (2015).
[21]Y. Kuwata and K. Suga, "Lattice Boltzmann direct numerical simulation of interface turbulence over porous and rough walls," Int. J. Heat Fluid Flow **61**, 145–157 (2016).
[22]Y. Kuwata and K. Suga, "Direct numerical simulation of turbulence over anisotropic porous media," J. Fluid Mech. **831**, 41–71 (2017).
[23]D.-Y. Maa, "Potential of microperforated panel absorber," J. Acoust. Soc. Am. **104**, 2861–2866 (1998).
[24]A. Silvestri, F. Ghanadi, M. Arjomandi, R. Chin, B. Cazzolato, and A. Zander, "Attenuation of turbulence by the passive control of sweep events in a turbulent boundary layer using micro-cavities," Phys. Fluids **29**, 115102 (2017).
[25]A. Silvestri, F. Ghanadi, M. Arjomandi, B. Cazzolato, and A. Zander, "Attenuation of sweep events in a turbulent boundary layer using micro-cavities," Exp. Fluids **58**, 58 (2017).
[26]W. K. Blake, "Turbulent boundary-layer wall-pressure fluctuations on smooth and rough walls," J. Fluid Mech. **44**, 637–660 (1970).
[27]N. D. Varano, "Fluid dynamics and surface pressure fluctuations of turbulent boundary layers over sparse roughness," Ph.D. thesis, Virginia Tech, 2010.
[28]T. Meyers, J. B. Forest, and W. J. Devenport, "The wall-pressure spectrum of high-Reynolds-number turbulent boundary-layer flows over rough surfaces," J. Fluid Mech. **768**, 261–293 (2015).
[29]L. A. Joseph, T. W. Meyers, N. J. Molinaro, and W. J. Devenport, "Pressure fluctuations in a high-Reynolds-number turbulent boundary layer flow over rough surfaces," AIAA 2016-2751, 2016.
[30]H. Bai, Kevin, N. Hutchins, and J. Monty, "Turbulence modifications in a turbulent boundary layer over a rough wall with spanwise-alternating roughness strips," Phys. Fluids **30**, 055105 (2018).
[31]S. A. Showkat Ali, M. Azarpeyvand, and C. R. Ilário da Silva, "Trailing-edge flow and noise control using porous treatments," J. Fluid Mech. **850**, 83–119 (2018).
[32]M. Mosallem, "Numerical and experimental investigation of beveled trailing edge flow fields," J. Hydrodyn., Ser. B **20**, 273–279 (2008).
[33]G. Ozkan, H. Akilli, and B. Sahin, "Effect of high porosity screen on the near wake of a circular cylinder," EPJ Web Conf. **45**, 01071 (2013).
[34]G. M. Ozkan and H. Akilli, "Flow control around bluff bodies by attached permeable plates," Int. J. Mech. Aerosp. Ind. Mechatron. Eng. **8**, 1035–1039 (2014).
[35]C. H. Bruneau and I. Mortazavi, "Numerical modelling and passive flow control using porous media," Comput. Fluids **37**, 488–498 (2008).
[36]H. Liu, J. Wei, and Z. Qu, "The interaction of porous material coating with the near wake of bluff body," J. Fluids Eng. **136**, 021302 (2014).
[37]J. E. J. Dupuit, *Etudes Theoriques et Pratiques sur le Mouvement des Eaux dans les Canaux de Couverts Etatravers les Terrains Permeables*, 2nd ed. (Dunod, 1863).
[38]P. Ligrani and P. Bradshaw, "Spatial resolution and measurement of turbulence in the viscous sublayer using subminiature hot-wire probes," Exp. Fluids **5**, 407–417 (1987).
[39]*Dantec Dynamics StreamWare Pro Installation and User Guide*, edited by Dantec Dynamics A/S (Dantec, 2013).
[40]N. Hutchins, T. B. Nickels, I. Marusic, and M. Chong, "Hot-wire spatial resolution issues in wall-bounded turbulence," J. Fluid Mech. **635**, 103–136 (2009).
[41]G. Corcos, "Resolution of pressure in turbulence," J. Acoust. Soc. Am. **35**, 192–199 (1963).
[42]S. Gravante, A. Naguib, C. Wark, and H. Nagib, "Characterization of the pressure fluctuations under a fully developed turbulent boundary layer," AIAA J. **36**, 1808–1816 (1998).
[43]F. Ghanadi, M. Arjomandi, B. S. Cazzolato, and A. C. Zander, "Analysis of the turbulent boundary layer in the vicinity of a self-excited cylindrical Helmholtz resonator," J. Turbul. **16**, 705–728 (2015).
[44]P. Schlatter and R. Orlu, "Assessment of direct numerical simulation data of turbulent boundary layers," J. Fluid Mech. **659**, 116–126 (2010).
[45]M. Goody, "Empirical spectral model of surface pressure fluctuations," AIAA J. **42**, 1788–1794 (2004).
[46]S. Berg, A. W. Cense, J. P. Hofman, and R. M. M. Smits, "Flow in porous media with slip boundary condition," paper presented at the International Symposium of the Society of Core Analysts, Calgary, Canada, 10–12 September 2007.
[47]P. Welch, "The use of fast Fourier transform for the estimation of power spectra: A method based on time averaging over short, modified periodograms," IEEE Trans. Audio Electroacoust. **15**, 70–73 (1967).
[48]C. K. Wentworth, "A scale of grade and class terms for clastic sediments," J. Geol. **30**, 377–392 (1922).